Robertson *et al.*
Journal of Neuroinflammation (2024) 21:238
https://doi.org/10.1186/s12974-024-03238-w

Journal of Neuroinflammation

RESEARCH

Open Access

Knockdown of microglial iron import gene, *Slc11a2*, worsens cognitive function and alters microglial transcriptional landscape in a sex-specific manner in the *APP/PS1* model of Alzheimer's disease

Katrina Volk Robertson[1], Alec S. Rodriguez[1], Jean-Philippe Cartailler[2], Shristi Shrestha[2], Michael W. Schleh[1], Kyle R. Schroeder[1], Arianna M. Valenti[1], Alec T. Kramer[3], Fiona E. Harrison[4*] and Alyssa H. Hasty[1,5*]

Abstract

Background Microglial cell iron load and inflammatory activation are significant hallmarks of late-stage Alzheimer's disease (AD). In vitro, microglia preferentially upregulate the iron importer, divalent metal transporter 1 (DMT1, gene name *Slc11a2*) in response to inflammatory stimuli, and excess iron can augment cellular inflammation, suggesting a feed-forward loop between iron import mechanisms and inflammatory signaling. However, it is not understood whether microglial iron import mechanisms directly contribute to inflammatory signaling and chronic disease in vivo. These studies determined the effects of microglial-specific knockdown of *Slc11a2* on AD-related cognitive decline and microglial transcriptional phenotype.

Methods In vitro experiments and RT-qPCR were used to assess a role for DMT1 in amyloid-β-associated inflammation. To determine the effects of microglial *Slc11a2* knockdown on AD-related phenotypes in vivo, triple-transgenic *Cx3cr1*$^{Cre-ERT2}$;*Slc11a2*$^{fl/fl}$;*APP/PS1*$^{+or-}$ mice were generated and administered corn oil or tamoxifen to induce knockdown at 5–6 months of age. Both sexes underwent behavioral analyses to assess cognition and memory (12–15 months of age). Hippocampal CD11b+ microglia were magnetically isolated from female mice (15–17 months) and bulk RNA-sequencing analysis was conducted.

Results DMT1 inhibition in vitro robustly decreased Aβ-induced inflammatory gene expression and cellular iron levels in conditions of excess iron. In vivo, *Slc11a2*^{KD} *APP/PS1* female, but not male, mice displayed a significant worsening of memory function in Morris water maze and a fear conditioning assay, along with significant hyperactivity compared to control WT and *APP/PS1* mice. Hippocampal microglia from *Slc11a2*^{KD} *APP/PS1* females displayed significant increases in *Enpp2*, *Ttr*, and the iron-export gene, *Slc40a1*, compared to control *APP/PS1* cells. *Slc11a2*^{KD} cells from *APP/PS1* females also exhibited decreased expression of markers associated with subsets of disease-associated microglia (DAMs), such as *Apoe*, *Ctsb*, *Ly9*, *Csf1*, and *Hif1a*.

*Correspondence:
Fiona E. Harrison
fiona.harrison@vumc.org
Alyssa H. Hasty
alyssa.hasty@vanderbilt.edu
Full list of author information is available at the end of the article

Conclusions This work suggests a sex-specific role for microglial iron import gene *Slc11a2* in propagating behavioral and cognitive phenotypes in the *APP/PS1* model of AD. These data also highlight an association between loss of a DAM-like phenotype in microglia and cognitive deficits in *Slc11a2*^{KD} *APP/PS1* female mice. Overall, this work illuminates an iron-related pathway in microglia that may serve a protective role during disease and offers insight into mechanisms behind disease-related sex differences.

Keywords Microglia, Iron, Inflammation, DMT1, Slc11a2, Alzheimer's disease, APP/PS1, Neuroinflammation, Sex differences, Behavior

Background

Alzheimer's disease (AD) is one of the most common neurodegenerative diseases and the most frequent cause of dementia. AD is primarily characterized by accumulation of extracellular amyloid-beta (Aβ) plaques and intraneuronal neurofibrillary tau tangles [1]. In addition to Aβ and tau, other pathological features have also been shown to contribute to AD development, including significant neuroinflammation, synaptic dysfunction, oxidative stress, and lysosomal dysfunction [2, 3]. Interestingly, emerging evidence demonstrates that excessive iron deposition in the brain is strongly associated with AD pathogenesis [4–6]. Iron levels in the brain increase significantly with age [7, 8] and the degree of iron load in disease-associated brain regions (i.e., the hippocampus and frontal cortex) positively correlates with aberrant protein aggregation and severity of cognitive decline [9–11]. Furthermore, iron has been found in dense core plaques and tau tangles in the brains of AD patients and mouse models [12–14], and directly binds to and exacerbates the toxicity of Aβ [15, 16]. Although iron is critical for myelination, neurotransmitter synthesis, and mitochondrial metabolism in the healthy brain, excessive iron can result in the harmful formation of toxic free radicals and production of reactive oxygen species (ROS), which can ultimately lead to lipid peroxidation, cellular damage, and ultimately cell death [17].

Microglia are resident innate immune cells of the central nervous system (CNS) and play essential roles in brain development, maintenance of neural homeostasis, and response to injury and disease in the CNS. While it is widely appreciated that microglial-mediated neuroinflammation is a key pathological hallmark of AD [18, 19], more recent work has also highlighted the prominent role microglia play in mediating brain iron dysregulation in disease [20–22]. Microglia are equipped with the necessary machinery to import, store, and export and/or recycle iron [20, 23, 24]. In fact, iron transport may occur preferentially in microglia compared to other cell types in the brain [25–27]. Despite their high capacity to handle and store iron, microglia are particularly susceptible to iron-induced damage [28] and Ryan et al. recently demonstrated a predominant role for microglia in mediating the harmful effects of excess iron on other neural cells in a tri-culture system [29]. Microglia are loaded with iron in AD and other neurodegenerative diseases, [30–34] and one of the key transcriptional changes in clusters of disease-associated microglia (DAMs) is an alteration in iron-storage genes such as *Fth1* and *Ftl* in both humans and mouse models of AD [35, 36]. While microglial iron loading has been more widely recognized as a key component of AD pathology, it is still not understood how this contributes to overall disease progression [5, 37, 38].

At the cellular level, an intimate relationship between microglial iron load and inflammatory signaling has been established. In a reciprocal manner, iron can enhance markers of inflammation and oxidative stress [21, 39, 40], and inflammatory signals induce the uptake and storage of iron [24, 41]. Specifically, microglia preferentially upregulate iron importer divalent metal transporter 1 (DMT1; gene name, *Slc11a2*) in response to acute inflammatory stimuli such as lipopolysaccharide (LPS) and Aβ [24, 41, 42]. DMT1 is a widely expressed proton-coupled ferrous iron (Fe^{2+}) importer found on the cellular plasma membrane and endosomal membrane [43]. This importer plays a role in transferrin-bound and non-transferrin-bound iron uptake, as it mediates the immediate import of ferrous iron at the cell surface, and also transports iron reduced in the endosome into the cytosol so it can be utilized by the cell [44]. In cell culture systems, inhibition of DMT1 results in a significant decrease in pro-inflammatory IL1β signaling in response to Aβ [45]. Furthermore, our work showed that knocking down *Slc11a2* blunts the neural inflammatory response to LPS in male, but not female, mice [42]. These results were observed in the absence of an additional iron load, suggesting a role for microglial DMT1 in helping to drive baseline inflammatory responses.

With these findings, it is intriguing to consider a role for microglial DMT1 in a disease of chronic cellular iron load and inflammation. To our knowledge, no studies have investigated whether targeting this microglial iron importer alters disease pathogenesis in vivo. We generated an inducible, microglial-specific genetic knockdown of *Slc11a2* in a model of AD in both male and female mice. We investigated whether microglial *Slc11a2*

knockdown alleviated markers of disease, including microglial inflammatory and oxidative stress markers and changes in behavior and cognition.

Materials and methods

Experimental animals

All mouse breeding, maintenance, and procedures were approved in advance and conducted in compliance with the Institutional Animal Care and Use Committee at Vanderbilt University. For the primary cell experiments from young and aged mice, young 9-week-old control C57BL/6 J male mice were purchased from Jackson Laboratories (Bar Harbor, ME, USA) (#000664, JAX). For aged mice, young C57BL/6J male mice were originally purchased from Jackson Laboratories and were aged and maintained in the Vanderbilt mouse facility until they were 27–30 months old. To determine the effect of decreased microglial DMT1 on disease, we generated a novel transgenic mouse model with inducible knockdown of *Slc11a2* in microglial cells in the *APP/PS1* model of AD. *Cx3cr1*$^{Cre-ERT2}$ mice (B6.129P2(C)-*Cx3cr1*$^{tm2.1(cre/ERT2)Jung}$/J; #020940) purchased from Jackson Laboratories (JAX, Bar Harbor, ME, USA) express a tamoxifen-inducible Cre-recombinase driven by the promoter for the microglial/macrophage *Cx3cr1* chemokine receptor gene, allowing for conditional knockdown of *loxP*-containing genes in *Cx3cr1*-expressing cells [46]. *Slc11a2- 'floxed'* mice (129S-*Slc11a2*^{tm2Nca}*/J;* #017789, JAX) [47] were bred with *Cx3cr1*$^{Cre-ERT2}$ homozygous mice to obtain *Slc11a2*$^{fl/fl}$*;Cx3cr1*$^{Cre++}$ homozygous animals. *APP/PS1*$^{+}$ hemizygous animals were purchased from JAX and maintained in our facility (Tg(APPswe,PSEN1dE9)85Dbo; MMRRC_034832-JAX). These transgenic animals express a chimeric mouse/human amyloid precursor protein (Mo/HuAPP695swe) and a mutant presenilin-1 (PS1-dE9), and have been widely used in AD research, particularly in relation to amyloid-β associated pathology [48–50]. We chose this model of AD based on the well-characterized development of disease-associated symptoms (i.e., amyloid deposition, cognitive deficits) and the progressive nature of disease development over the course of several months. This slower onset compared to other models allows us to examine the early pathological changes that occur prior to the onset of symptoms later in the course of disease. Additionally, the *APP/PS1* model has already been shown to exhibit significant microglial iron loading [21, 32], and an amyloid-driven model is relevant based on associations between iron and Aβ in the brain [15, 51]. *APP/PS1*$^{+}$ hemizygous animals were bred separately with *Slc11a2*$^{fl/fl}$ animals to yield *Slc11a2*$^{fl/fl}$*;APP/PS1*$^{+}$ mice. Resulting progeny from these crosses were then bred with *Slc11a2*$^{fl/fl}$*;Cx3cr1*$^{Cre-ERT2++}$ animals to yield triple-transgenic *Slc11a2*$^{fl/fl}$*;Cx3cr1*$^{Cre-ERT2\pm}$*;APP/PS1*$^{+}$ or *APP/PS1*$^{-}$ (i.e., 'WT') mice (Additional File 1A). All mice used in experiments were *Slc11a2*$^{fl/fl}$*;Cx3cr1*$^{\text{Cre}-\text{ERT2}\pm}$ and either *APP/PS1*$^{+}$ hemizygotes or WT as littermate controls. Experimental mice were on a mixed 129S/BL6 background, with > 80% BL/6J genetic makeup as confirmed via Transnetyx strain analysis (Cordova, TN). All genotypes were confirmed with an ear snip via Transnetyx using real-time PCR. Mice were weaned at 3 weeks of age and had ad libitum access to food (*LabDiets*, standard rodent chow 5001, 240 ppm iron) and water. Both male and female mice were used in our experiments and were group-housed (2–5 per cage) by sex in transparent cages at 22–25 °C under a 12 h light/dark cycle in a specific pathogen-free facility. Control and experimental animals were randomly assigned across cages.

Tamoxifen treatment

Tamoxifen (Sigma #T5648) was dissolved in corn oil (Sigma #C8267-2.5L, lot #MKCK6411, Saint Louis, MO) to generate a 20 mg/mL stock concentration by sonicating the mixture and stirring overnight in a glass vial at 37 °C. *Slc11a2*$^{fl/fl}$*;Cx3cr1*$^{Cre-ERT2\pm}$*;APP/PS1*$^{+\ or\ -}$ male and female mice at 5–6 months of age were administered a dose of 4 mg (maximum 200 µL volume) tamoxifen via oral gavage every day for five consecutive days [42, 52] (Additional File 1B). All mice that received tamoxifen are denoted as '*Slc11a2*$^{\text{KD}}$', and are either *APP/PS1* or WT. Littermate mice with the same genotypes (*Slc11a2*$^{fl/fl}$*;Cx3cr1*$^{Cre-ERT2\pm}$*;APP/PS1*$^{+\ or\ -}$) were administered gavage with corn oil as a control for the presence of Cre based on work showing effects of *Cx3cr1*$^{\text{Cre}-\text{ERT2}}$ genotype alone on microglial function [53, 54]. Corn-oil-treated animals are denoted as 'Control,' and are either *APP/PS1*$^{+}$ *or* WT. The numbers of experimental animals used are shown in Supplemental Table 1 of Additional File 2. We chose to induce knockdown of *Slc11a2* between 5–6 months of age in these mice, as it is a relatively early timepoint in this AD model when Aβ plaque deposition becomes visible and allowed us to assess the effect of early changes in microglial *Slc11a2* on downstream disease development. Knockdown of *Slc11a2* was confirmed in isolated microglia from all animals via RT-qPCR utilizing a primer targeting *Slc11a2* exons 6–8 (Additional File 1C).

Behavioral assays

All behavioral assays were conducted in the Vanderbilt Murine Neurobehavioral Core after mice were acclimated to the facility for at least one to 2 weeks. All mice underwent testing between 12 and 15 months of age (mouse numbers and body weights shown in Additional File 2, Supplemental Table 1 and Supplemental Table 2). Control WT and *APP/PS1* mice were randomly

distributed across cages and litters, and the order of mice run through each assay was also randomly assigned. To avoid experimenter bias, mice of both sexes and all four experimental groups were evenly and randomly split between two different experimenters of opposite sex, who were blinded to the genotype and treatment of the mice before testing. The running order of assays was kept consistent for all animals in each study, and animals were run at the same time each day between 0630 and 1300 h with one task per day. For each task, mice were acclimated to the testing room for 30 min to 1 h prior to testing, and control and experimental groups were evenly and randomly distributed across cages, days, and time of each assay. Following completion of a trial, each apparatus was cleaned of feces, disinfected, and deodorized with an anti-bacterial spray (Peroxigard, Virox Technologies) in between animals. *APP/PS1*$^{+}$ mice are known to be prone to spontaneous seizures [55] and any mouse that exhibited a seizure during an assay was excluded from that analysis ($n=3$ male *Slc11a2*^{KD} *APP/PS1*$^{+}$). Additionally, two mice died spontaneously prior to completion of all tasks and euthanasia (one male *Slc11a2*^{KD} *APP/PS1* and one female Control *APP/PS1*). The data for these animals is recorded for the tasks completed prior to death.

Nest building

As a measurement of general cognition and well-being, an overnight nest building assay was used. Nest building assessments were performed as the first behavioral task to minimize effects of stress on the mice from other behavioral assays. Mice were single-housed and given 5 g of cotton nestlet (Ancare, Bellmore, NY) in the afternoon the day prior. The next morning, amount shredded and quality of nests was scored by a blinded observer using a 0–5 scale adapted from previous work, in 0.5 increments [42, 56, 57]. Following nest building assessment, mice were re-housed in groups of 4–5 before all other behavioral tasks.

Locomotor activity: elevated zero maze and open field

Several assays were used as control measures of anxiety and for locomotor activity assessment. An elevated zero maze (white maze, width 5 cm; diameter 50 cm; wall height 15 cm, Stoelting Co. IL) was used first, where mice underwent a single 5 min trial of free exploration. Mice were video-recorded using a ceiling-mounted camera and movement was automatically tracked and scored using AnyMaze (Stoelting Co., Wood Dale, IL). Analysis parameters were set to ensure 80% of the mouse needed to be present in either the 'open' or 'closed' zone for an entry into that zone to be recorded. Total time in the open and closed zones and total distance traveled were measured. Sound-attenuating transparent open field chambers (27.5 × 27.5 cm) were used for a second measurement of baseline locomotor activity. Mice were placed in the center of the chamber and allowed to explore freely for 45 min. Distance traveled was recorded automatically via the breaking of infrared beams (MedAssociates ENV-510 software, Fairfax, VT). Additionally, time spent in the center area (19.05 × 19.05 cm) versus time in the 'surround' was calculated as a control measure of anxiety-like behavior.

Short-term spatial working memory

A single-trial Y-maze was used as another measurement of baseline locomotor and exploratory behavior, as well as an assay to measure short-term working memory function. A clear plexiglass three-arm Y-maze (each arm 5 cm in width, 34.5 cm long) with differentiated arms (different colors of paper with or without patterns placed underneath the maze) was used. All mice were placed in the same point of the same arm and allowed to freely explore for 6 min. A ceiling-mounted camera recorded video of the mice and AnyMaze automatically measured total distance traveled and order of arm entries. Entry into another arm was predicated on having at least 80% of the mouse cross into at least 1 cm of the arm. Spontaneous alternation as a measure of intact working memory was calculated by hand using arm entry order data from AnyMaze. A 'correct' alternation is defined by three consecutive entries into three different arms (e.g., ABC, BCA, CAB). Percent alternation was calculated using: ((Number of spontaneous alternations) / (Number of total arm entries—2)) * 100.

Morris water maze

Mice underwent testing in the Morris water maze (MWM) to assess the effect of *Slc11a2* knockdown on learning and memory [58]. Briefly, a circular pool approximately 1 m in diameter filled approximately 30 cm deep with 22–27 °C water was used for this task. A white round platform (10 cm in diameter) was used to provide animals an escape from the water. Mice first underwent two visual training days, where the platform jutted above the water with a pole attached to allow mice to see the target platform. This platform was moved around to each of the four quadrants on each session during training days to allow the opportunity for each animal to swim and survey the room, which contained multiple visual spatial cues kept constant throughout. Each training day comprised four trials per mouse, and each mouse was given 60 s to find the platform. If a mouse did not reach the platform in 60 s, it was guided to and placed on the platform for at least 5 s. On subsequent days following the two visual training days, the water was made opaque with non-toxic tempura white paint, and the platform

was submerged approximately 0.5 cm under the water. The platform was kept in the same location for each trial and day, and mice were randomly placed in different locations in the pool so that the use of spatial cues for navigation was necessitated. Mice underwent four trials per day for 5 days, with each trial lasting 60 s to assess learning and short-term memory. If mice did not find the platform within 60 s, they were guided to the platform and escape latency was recorded as 60 s. Following the final day of testing, the platform was removed and mice were allowed to swim freely for 60 s. Total time spent in the target quadrant where the platform used to be, time spent around the location of the platform, swim speed, total distance traveled, and time spent in perimeter were recorded as measurements of platform location memory.

Fear conditioning assay

Following completion of all other behavioral tasks, a fear conditioning assay was conducted to assess differences in fear-associated memory. Mice were placed in sound-attenuating chambers with a wire grid floor. On the 1st day (training trial), mice were placed in the chambers for 8 min and allowed to explore freely. Every 2 min, a 30 s tone was played, followed immediately by a small shock administered through the wire floor (1 s, 0.5 mA). This tone-shock pairing occurred 3 times during the training trial. To assess contextual fear conditioning, mice were placed back into the same chamber the next day and allowed to run around freely for 4 min with no tone or shock presented. Total time freezing—indicative of fear memory—was recorded automatically (VideoFreeze, MedAssociates). To assess cued fear conditioning (memory of the tone), mice underwent a second testing trial. This trial included a different experimenter handling the mice, significant alterations to the chamber with white walls, white floor inserts, and red light, and the scent of vanilla placed in an open tube outside the chamber. Mice freely explored the chamber for 2 min before the tone was administered for the final 2 min (without a shock pairing). Total time spent freezing during the no-tone and tone segments were recorded as a measurement of cued fear memory.

Mouse euthanasia and tissue collection

At the time of euthanasia, mice were deeply anesthetized with isoflurane and 500–700 µL of blood was collected via cardiac puncture. Immediately following blood collection, mice were trans-cardially perfused with 20 mL of cold 1 × Dulbecco's phosphate-buffered saline (DPBS) to remove circulating blood and decapitated for rapid brain removal. Whole brains were either placed on ice for mincing and processing for cellular isolation, or bilateral hippocampus was isolated first before proceeding to cellular isolation.

Tissue digestion and single-cell suspension preparation

Brains were rapidly removed and briefly placed in 3 mL cold, sterile 1 × Hank's buffered saline solution (HBSS, Gibco, #14175095) containing 1% fetal bovine serum (FBS, heat-inactivated; Gibco, #10082147) to remove any residual blood. Microglia isolation was performed following published protocols, with slight modifications [59–61]. Briefly, whole brains were transferred and finely minced with scissors in cold, sterile "IMG media" [Dulbecco's modified Eagle's medium (DMEM) with high glucose (4.5 g/L) and L-glutamine media (Gibco, #11965092) containing 10% FBS and 1% penicillin–streptomycin (Gibco, #15140122). Minced tissue was transferred into 50 mL conical tubes and 5 mL of digestion media (IMG media + 100 units Papain, #LK003176; 500 Kunitz units DNase, #LK003170, Worthington Biochemicals, Lakewood, NJ) was added to each tube. Whole-brain samples were enzymatically-dissociated by placing in an orbital shaker for 1 h at 37 °C, diluted with 10 mL IMG media, and strained through 70 µm sterile filters (Corning, #431751). Bilateral hippocampus samples in the RNA-sequencing studies were treated in the same manner described above, with slight modification. Bilateral hippocampus samples were isolated and immediately placed in 15 mL conical tubes on ice and 2.5 mL digestion media was added. Samples were incubated for 30 min in an orbital shaker at 37 °C. Every 10 min, samples were triturated up and down with a serological pipette of decreasing size before straining samples through filters and proceeding with subsequent steps. All samples were further processed at 4 °C unless otherwise indicated.

Percoll gradient

Cells were centrifuged for 5 min at 500 × *g*, re-suspended in a solution of 30% isotonic Percoll and IMG media (Cytiva, #17-0891-01), and slowly layered onto a 70% Percoll gradient with HBSS + 1% FBS. HBSS + 1% FBS (without Percoll) was layered on top, and samples were centrifuged for 15 min at room temperature at 600 × g with the brake set to the lowest setting to allow for density separation. The supernatant containing myelin and neuronal debris was removed, and cells at the interface between the 30–70% gradients were carefully collected and placed on ice into 8 mL HBSS + 1% FBS in a fresh tube to wash residual Percoll. Cells were centrifuged at 500 × *g* for 5 min at 4 °C, and pelleted cells were re-suspended in appropriate media for downstream assays.

Plating and treatment for primary cell experiments

For experiments conducted in isolated primary cells from young and aged mice, all steps above were performed under sterile conditions in a cell culture hood with autoclaved tools and sterile-filtered reagents. Mixed glial cells isolated and pelleted from the Percoll gradient were re-suspended in 1 mL IMG media for counting and plating. Cells were counted using the Nexcelom Cellometer Auto T4 Cell Counter (Nexcelom Biosciences) and plated at a density of 100,000 cells per well in poly-L-lysine-coated 48-well plates in pre-warmed sterile IMG media containing 5 ng/mL GM-CSF (R&D Systems, #415-ML-010). Media was changed the next day, and then every other day for 5 days before stimulation with Aβ as described below.

CD11b immunomagnetic microglial isolation

For experiments analyzing gene expression (RNA-sequencing and RT-qPCR) in microglia from the triple-transgenic animals, Percoll-isolated glial samples were further processed for enrichment of $CD11b^+$ microglia. Following Percoll gradient separation, centrifugation, and pelleting, cells were re-suspended in 400 µL cold "MACS" buffer (1×PBS containing 0.5% FBS and 2 mM EDTA) and transferred to 5 mL tubes. Cells were centrifuged at 4 °C for 5 min at 500×*g*, pelleted, and re-suspended in 90 µL MACS buffer for magnetic labeling and separation according to manufacturer's instructions (Miltenyi Biotec, Bergisch Gladbach, Germany). Briefly, samples were incubated with magnetic anti-CD11b MicroBeads (Miltenyi Biotec, #130-093-634; 10 µL per 90 µL buffer/brain) for 15 min at 4 °C. Magnetic separation was performed utilizing MS columns, and $CD11b^+$ cells and the effluent non-magnetic fractions ($CD11b^-$ cells) were obtained. Following a final centrifugation for 5 min at 500×*g*, cells were immediately re-suspended in RLT lysis buffer (Qiagen, #74004) supplemented with 1% beta-mercaptoethanol, briefly vortexed, and flash-frozen in liquid nitrogen. Samples were stored at −80 °C until RNA isolation.

In vitro cells and experimental treatments

The immortalized microglial cell line, "IMG" [62], was used for in vitro experiments to assess the direct effect of pharmacological inhibition of DMT1 on Aβ-induced inflammation. IMG cells were purchased from Millipore (Cat. #SCC134, RRID:CVCL_HC49), and cultured as described using Accutase for dissociation and passaging [45]. Briefly, cells were cultured up to a maximum of 10 passages in sterile Dulbecco's modified Eagle's medium (DMEM) with high glucose (4.5 g/L) + 2.5 mM glutamine (Gibco, #11965092) supplemented with 10% fetal bovine serum (FBS, heat-inactivated, Gibco, #16140071) and 1% penicillin/streptomycin ("IMG media").

Ebselen treatments

The drug ebselen [2-phenyl-1,2-benzisoselenazol-3(2*H*)-one] was chosen as a robust inhibitor of DMT1 [63]. Ebselen was purchased from Focus Biomolecules (#10-2288) and re-suspended in sterile dimethyl sulfoxide (DMSO; Sigma, #276855). IMG cells were plated and grown overnight in six-well-plates (150,000–200,000 cells/well) in IMG media. The next day, cells were treated for 24 h with either 25 µM ebselen or control DMSO. This concentration of ebselen was chosen as the treatment dose following preliminary experiments indicating this dose decreased cellular iron content and following similar reported doses from previous work [64]. Following 24 h of ebselen/DMSO treatment, cells were further treated as described below.

Aβ and iron treatments

In both IMG cells and primary isolated microglia in the young and aged mice experiments, oligomeric $A\beta_{1\text{-}42}$ was used as an acute AD-associated inflammatory stimulus. Aβ (HFIP-treated, rPeptide #A-1163-2) and scrambled Aβ (rPeptide #A-1004-2) were purchased from rPeptide and 5 mM stock solutions were prepared with sterile, anhydrous DMSO (Sigma #276855) and sonicated for 15 min before storing aliquots at − 20 °C. The day before cell stimulation, oligomeric $A\beta_{1\text{-}42}$ was prepared as previously described [39] using cold, sterile phenol-free Ham's F-12 media (R&D Systems, #M25350) and allowed to rest at 4 °C for 24 h. The next day, cells were treated with 1 µM $A\beta_{1\text{-}42}$ or scrambled Aβ for 24 h before lysis and collection for RNA isolation. For in vitro experiments in IMG cells, ferric ammonium citrate (FAC, Sigma, #F5879) was used as a non-transferrin-bound form of iron. FAC was re-suspended fresh in sterile RNase-free water immediately before each experiment, and cells were treated for 24 h with 50 µM FAC based on literature recommendations [39, 65] or water (control), with or without Aβ prior to lysis and collection for RNA isolation or ICP-MS, as described below.

Inductively-coupled plasma mass spectrometry (ICP-MS)

Following 24 h of treatment with scrambled Aβ or 1 µm $A\beta_{1\text{-}42}$ ± FAC, IMG cells were collected for ICP-MS analysis of intracellular iron content. After washing twice with ice-cold 1×PBS, cells were collected into metal-free tubes using Accutase, and total cell counts were measured for data normalization. After centrifugation at 600xg for 5 min and removal of supernatant, cells were acid-digested in 150 µL trace-metal grade nitric acid (70%, OPTIMA Grade HNO_3, Fisher-Sci, #A467-250), and 30% ultra trace-grade hydrogen peroxide (Thermofisher) was added at a 1:4 dilution (37.5 µL H_2O_2). Samples were vortexed, incubated at 65 °C overnight, and

diluted the next day with Ultrapure Milli-Q water (Ω18.2) at 10 times the volume of nitric acid (1.5 mL water). ICP-MS was performed at the Vanderbilt Mass Spectrometry Research Center using an Agilent 7700 ICP-MS (Agilent) attached to a Teledyne autosampler (CETAC Technologies, Omaha, NE). The following settings were used: cell entrance = − 40 V, cell exit = − 60 V, plate bias = − 60 V, OctP bias = − 18 V, and collision and cell helium flow = 4.5 mL/min. Samples were introduced by peristaltic pump and taken up at 0.5 rps for 30 s, followed by 30 s at 0.1 rps for signal stabilization. A calibration curve for each isotope was made at 0, 1, 10, 100, 1000, 5000, and 10,000 ppb, and blanks were run following standard calibration to wash out signal from the 10,000 ppb standard. Data were acquired and analyzed using the Agilent Mass Hunter Workstation Software version A.01.02.

RNA isolation, cDNA synthesis, and RT-qPCR

Lysed cell samples from all experiments (i.e., $CD11b^+$ microglia and primary isolated glia) were processed for total mRNA using an RNeasy Micro Kit with DNase treatment according to manufacturer's instructions (Qiagen, Hilden, Germany, #74004), with the exception of the IMG experiments, which used the RNeasy Mini Kit (Qiagen, # 74104). Following on-column RNA purification and elution, cellular RNA was reverse transcribed into cDNA at equal concentrations across samples using iScript Reverse Transcriptase (BioRad, Hercules, CA). RT-qPCR was conducted to assess the expression of several genes and confirm *Slc11a2* knockdown using FAM-conjugated TaqMan Gene Expression Assay primers (Thermofisher, shown in the table in Additional File 3) and iQ Supermix (BioRad). PCR reactions were performed in duplicate under thermal conditions: 95 °C for 10 min, followed by 40 cycles of 95 °C for 15 s, and 60 °C for 45 s. The expression of each gene was normalized to a housekeeping gene (either *18S* or *ActinB* where indicated), and relative expression values were analyzed utilizing the comparative cycle threshold $2^{-\Delta\Delta CT}$ method [66].

RNA sequencing and library preparation

Following on-column purification and DNase treatment with the Qiagen RNeasy Micro Kit, total mRNA extracted from hippocampal $CD11b^+$ samples was submitted to the Vanderbilt Technologies for Advanced Genomics (VANTAGE) Core facility for sample quality control assessment and RNA-sequencing (RNA-seq). Only hippocampal $CD11b^+$ microglia isolated from female animals were used for RNA-seq, following earlier findings of significant behavioral differences primarily in $Slc11a2^{KD}$ female *APP/PS1* animals. The concentration of RNA samples was determined by NanoDrop (ThermoScientific). Sample Quality Control analysis was assessed using fluorometry Qubit and integrity by BioAnalyzer, and a RIN value of > 7 was confirmed for all samples before proceeding to library preparation and sequencing. Paired-end sequencing libraries were constructed using a standard mRNA NEBNext Poly(A) selection Library Prep Kit (Illumina). Library Quality Control analysis was performed by using Qubit and BioAnalyzer to determine the concentration and size bp. Samples were then sequenced at multiplex Paired-End 150 bp using the Illumina NovaSeq 6000 sequencing platform. To confirm sequencing quality, Illumina Quality Scores were calculated utilizing the following equation: $Q = -10\log_{10}I$. All samples sequenced reached sequencing quality of at least Q30.

Sequencing analysis: alignment, mapping, quantification, differential expression

Gene alignment, read mapping, gene counts quantification, and differential gene expression analyses were conducted at the Creative Data Solutions (CDS) Core at Vanderbilt. RNA-seq reads were adapter-trimmed and quality-filtered using Trimgalore v0.6.7 [67] and Cutadapt 1.18 [68] to remove adapter sequences and pairs that were either shorter than 20 bp or that had Phred scores less than 20. An alignment reference was generated from the mm39 mouse genome and GENCODE comprehensive gene annotations (M31), to which trimmed reads were aligned and counted using Spliced Transcripts Alignment to a Reference (STAR) v2.7.9a [69] with the –quantMode GeneCounts parameter. About 30–50 million uniquely mapped reads were acquired per sample. DESeq2 package v1.36.0 [70] was used to perform sample-level quality control, low count filtering, normalization and downstream differential gene expression analysis. Genomic features counted fewer than five times across at least three samples were removed. The default significance cutoff (0.1) for optimizing the independent filtering in DESeq2 was also used.

The measure of standard deviation (sd) and quantiles on principal component 1 (PC1) among samples was used to assess whether any samples were a statistical outlier. One sample in the Control *APP/PS1* group was removed from analyses after exhibiting a deviation of > 2 standard deviations and an interquartile range of > 1.5 in PC1 compared to its respective group (sample shown in Additional File 4B and C). Five to six biological replicates per condition were included for the differential expression analysis. Differentially expressed genes were identified using a false discovery rate (FDR) adjusted p-value threshold of 0.05, calculated using the Benjamini-Hochberg (BH) procedure for multiple hypothesis testing correction, and a log2 fold change threshold of greater

than 1. Gene set enrichment analysis (GSEA) [71] was performed using the R package Clusterprofiler [72] with gene sets from the Mouse MSigDB database [73]. Coverage of reads across annotated exons in the *Slc11a2* gene analysis was done using the R package ggcoverage 1.3.0 [74]. All data processing was performed at the Advanced Computing Center for Research and Education (ACCRE) at Vanderbilt University.

Data and statistical analyses

Data are presented as mean ± S.E.M. All experiments were analyzed using analysis of variance (ANOVA) for multiple comparisons followed by appropriate post-hoc analyses unless otherwise noted. Male and female data were first compared using ANOVA (2(Sex) × 2(Genotype) × 2(Treatment), followed by Sidak's corrections for multiple comparisons and analysis of interaction effects. Based on our previous work showing sex differences in *Slc11a2* expression between males and females, most primary analyses were conducted within each sex separately to assess the effect of *Slc11a2* knockdown in each sex. To do this, a 2(Genotype) × 2(Treatment) ANOVA followed by Sidak's corrections was used. In analyzing MWM data, repeated measures ANOVA (2(Knockdown) × 2(*APP/PS1* Genotype) × 5(Day)) was used to analyze latency data from multiple training days and Tukey's post-hoc analysis was used following significant F values to establish differences among all groups. Data from primary cell and IMG cell experiments were analyzed using either 2(Treatment) × 2(Age) ANOVA or 3(Treatment) × 2(ebselen/DMSO) ANOVA, respectively. Sidak's post-hoc analysis was used for interaction effects and corrections for multiple comparisons. Statistical outliers within each group for all studies were identified using either the ROUT or Grubb's method for outliers and excluded from statistical analyses. GraphPad Prism 9 (GraphPad Software, San Diego, CA, USA) was used for statistical analyses outside of RNA-seq analyses conducted in R. Differences among groups were considered significant at values of $p < 0.05$.

Results

Summary

The data presented are from experiments in primary microglia isolated from young and aged mice treated with Aβ in vitro, immortalized IMG cells treated with a DMT1 inhibitor followed by Aβ and iron, and data from a triple-transgenic AD mouse model with microglial *Slc11a2* knockdown in both sexes. These experiments were designed to examine relationships between Aβ and microglial DMT1 at the cellular level, to directly target DMT1 in vitro to examine changes at the molecular level, and to determine the effects of targeting microglial *Slc11a2*/DMT1 at the behavioral level.

Age and Aβ stimulation synergize to increase microglial *Slc11a2* and iron loading markers in primary microglia

To assess a potential role for microglial iron and *Slc11a2* in aging and Aβ-related pathology, we first isolated microglia from young (nine-week-old) and aged (two-year-old) mice for primary cell experiments. We observed significant ferritin (FtL) protein deposits in microglia isolated from aged compared to young mice (Fig. 1A), demonstrating, as others have shown, a key iron-loading microglial phenotype in aging [38, 75]. To determine whether *Slc11a2* contributes to this age-associated increase in iron and whether the transporter gene plays a role in Aβ-related disease conditions, isolated cells from young and aged mice were treated in vitro with an acute stimulus of 1 μM oligomeric Aβ for 24 h and gene expression of *Slc11a2* was measured. As others have also shown [24, 45], there was a significant increase in microglial *Slc11a2* in response to acute Aβ exposure (Fig. 1B, *Treatment,* $F(1,35) = 48.91$, $p < 0.0001$). Additionally, cells from the two-year-old aged mice exhibited an augmented Aβ-induced *Slc11a2* response, which was significantly greater than the response observed in the cells from young mice (*Age,* $F(1,35) = 11.21$, $p = 0.002$; young vs. old Aβ, $p = 0.005$). In addition, there was a robust increase in the expression of pro-inflammatory cytokines *Tnfα, Il1β,* and *Il6* in response to Aβ (Fig. 1C–E, *Il6: Treatment,* $F(1,32) = 41.20$, $p < 0.0001$; *Il1β:* $F(1,34) = 24.23$, $p < 0.0001$; *Tnfα:* $F(1,34) = 77.83$, $p < 0.0001$), which was even greater in the cells from the aged mice compared to those isolated from the young mice (significant for *Tnfα: Age,* $F(1,34) = 6.52$, $p = 0.015$, *Interaction* $F(1,34) = 5.57$, $p = 0.024$; young vs. aged Aβ $p = 0.005$). Along with differences in Aβ-induced *Slc11a2* gene levels, there was a significant increase in iron-storage genes *Ftl* and *Fth1* in response to Aβ only in the cells from the aged animals (Fig. 1F, G). Specifically, Aβ induced an increase in *Fth1* in the aged glia (*Age,* $F(1,29) = 12.46$, $p = 0.001$, *Treatment,* $F(1,29) = 13.67$, $p = 0.0009$), and *Fth1* and *Ftl* were significantly higher in response to Aβ in the aged cells when compared to the young cells (*Fth1,* young vs. aged, $p = 0.01$; *Ftl: Age,* $F(1,34) = 7.92$, $p = 0.008$, young vs. aged, $p = 0.02$). There were no differences in expression of *Tfrc*—another main iron importer gene—due to age or Aβ treatment (Fig. 1H, $p > 0.05$), suggesting that a specific gene expression increase in *Slc11a2* may accompany age- and Aβ-related changes in cellular iron and inflammatory status. Aβ also decreased *Slc40a1* (gene for ferroportin, main iron exporter) to a similar degree in the cells from the young and aged animals (Fig. 1I, *Treatment,* $F(1,30) = 23.40$, $p < 0.0001$), further suggesting that a specific alteration in *Slc11a2* in response to age and Aβ may be involved in the progression of disease.

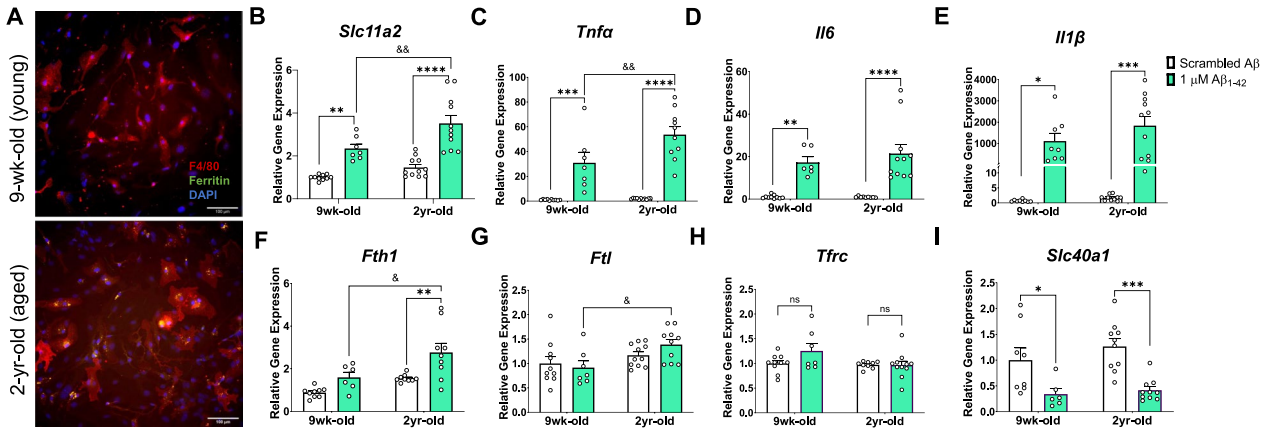

Fig. 1 Age and Aβ stimulation synergize to increase microglial *Slc11a2* and iron-loading markers in primary microglia. **A** Representative images of Percoll-isolated glia from a young (top image, 9-week-old) and aged (bottom image, 2-year-old) mouse showing ferritin deposits in microglia from the aged mouse. Isolated glia were stained with antibodies raised against ferritin-L and F4/80, along with DAPI to visualize ferritin, microglia, and nuclei, respectively. Images shown at 20x, scale bar = 100 μm. **B**–**I** Relative gene expression (compared to control scrambled Aβ) of (**B**) *Slc11a2,* **C** *Tnfa,* **D** *Il6,* **E** *Il1β,* **F** *Fth1,* **G** *Ftl,* **H** *Tfrc,* and **I** *Slc40a1* via RT-qPCR. Isolated cells from young and aged mice were plated and treated with scrambled Aβ or 1 μM $Aβ_{1-42}$ for 24 h before collection for RNA isolation and RT-qPCR analysis. Two-way ANOVA, *p < 0.05, **p < 0.01, ***p < 0.001, ****p < 0.0001 effect of treatment. $^{\&}$p < 0.05, $^{\&\&}$p < 0.01 effect of age x treatment. *ns* not significant. Data represent the mean ± S.E.M of 7–11 mice per group. Statistical outliers were removed using the Grubb's test

DMT1 inhibition in vitro significantly blunts Aβ-induced inflammatory markers and decreases cellular iron levels in immortalized microglia

Based on the purported roles for DMT1 during Aβ stimulation and iron load observed in our aged primary cell experiments, we assessed the effect of directly inhibiting DMT1 on Aβ and iron-induced inflammation in a microglial in vitro system. Cells from the murine immortalized microglial cell line, "IMG" cells [62], were treated with ebselen, a pharmacological inhibitor of DMT1 [63], before subsequent treatment with scrambled Aβ, oligomeric $Aβ_{1-42}$ alone, or iron (50 μM FAC) + $Aβ_{1-42}$. Aβ stimulation led to a robust increase in microglial pro-inflammatory *Il1β, Il6, Tnfα, Egr1,* and *Nos2* transcription, as expected (Fig. 2A–D**,** *Il1β: Treatment,* $F(3,22) = 16.78$, $p < 0.0001$; *Il6: Treatment,* $F(3,23) = 5.28$, $p = 0.006$; *Tnfα: Treatment,* $F(3,23) = 10.89$, $p = 0.0001$; *Egr1: Treatment,* $F(3,21) = 6.72$, $p = 0.002$, *Nos2: Treatment,* $F(3,23) = 16.31$, $p < 0.0001$). Addition of 50 μM FAC did not have a significant effect on Aβ-induced inflammatory markers. Ebselen profoundly decreased the Aβ-induced pro-inflammatory response for all three cytokines assayed along with *Egr1* and *Nos2*, even in the absence of excess iron added to the media (Aβ alone condition) (Fig. 2A–E**,** *Il1β: Interaction,* $F(3,22) = 15.76$, $p < 0.0001$; *Il6: Interaction,* $F(3,23) = 4.81$, $p = 0.0096$; *Tnfα: Interaction,* $F(3,23) = 6.89$, $p = 0.0018$; *Egr1: Interaction,* $F(3,21) = 6.01$; *Nos2: Interaction,* $F(3,23) = 13.18$, $p < 0.0001$). Markers typically associated with anti-inflammatory and homeostatic microglial subtypes such as *Mrc1* and *Cx3cr1* were significantly decreased due to Aβ treatment, although ebselen treatment did not exert an additional effect (Fig. 2F, G**,** *Mrc1: Treatment,* $F(3,22) = 7.42$, $p = 0.001$; *Cx3cr1: Treatment,* $F(13,22) = 17.10$, $p < 0.0001$.) Aβ induced a significant upregulation in *Slc11a2* and ebselen inhibited this increase when a bolus of FAC was added as well (Fig. 2H**,** *Treatment,* $F(3,23) = 5.07$, $p = 0.008$, *Interaction,* $F(3,23) = 3.49$, $p = 0.032$). This was paralleled by a change in *Fth1* levels in ebselen-treated cells (*Interaction,* $F(3,22) = 4.23$, $p = 0.016$), as well as a decrease in total intracellular iron levels as measured via ICP-MS, where ebselen significantly decreased cellular iron levels in the FAC+$Aβ_{1-42}$ condition (Fig. 2J**,** *Treatment,* $F(3,16) = 72.53$, $p < 0.0001$, *Ebselen,* $F(1,16) = 4.15$, $p = 0.058$, *Interaction,* $F(3,16) = 3.52$, $p < 0.05$). These data demonstrate associations between DMT1 inhibition, decreases in cellular iron levels, and blunted Aβ-induced pro-inflammatory responses in IMG cells.

Microglial *Slc11a2* knockdown results in a hyperactive phenotype in female *APP/PS1* mice and worsens hyperactivity in male *APP/PS1* mice at 12–15 months

To determine the effects of knocking down *Slc11a2* in vivo, we generated a transgenic mouse line allowing for inducible knockdown of *Slc11a2* in microglia between 5 and 6 months of age. Between 7 and 9 months after tamoxifen treatment, when mice were 12–15 months of age, male and female control WT, control *APP/PS1*, $Slc11a2^{KD}$ WT, and $Slc11a2^{KD}$ *APP/PS1* mice were run through a series of behavioral assays to assess the effect

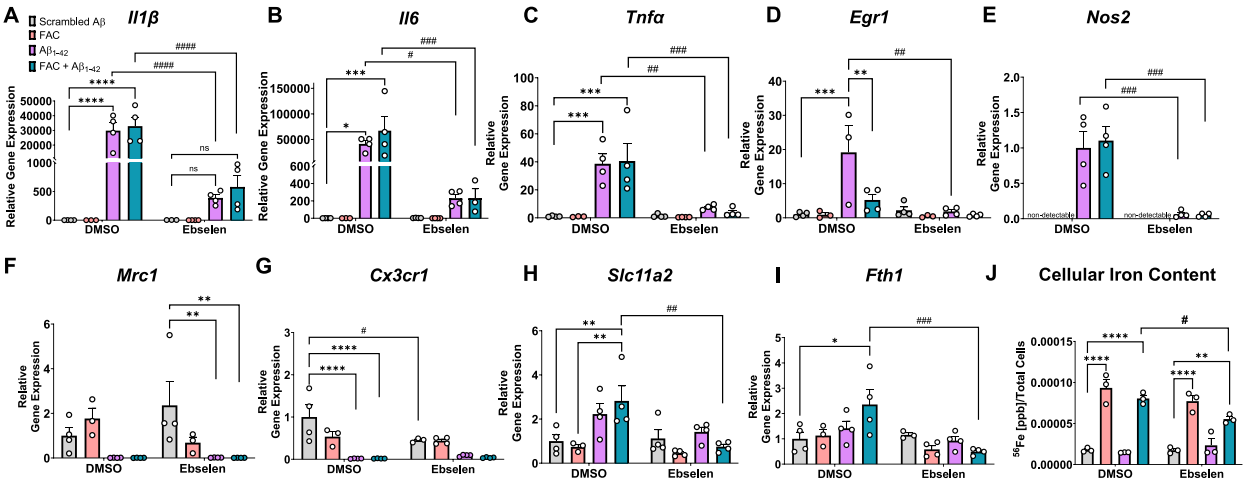

Fig. 2 DMT1 inhibition in vitro significantly blunts Aβ-induced inflammatory markers and decreases cellular iron levels in immortalized microglia. **A**–**I** Relative gene expression (compared to scrambled Aβ DMSO) via RT-qPCR of **A** *Il1β,* **B** *Il6,* **C** *Tnfa,* **D** *Egr1, E Nos2,* **F** *Mrc1,* **G** *Cx3cr1,* **H** *Slc11a2,* and **I** *Fth1* in IMG cells. IMG cells were treated for 24 h with DMSO or 25 μM ebselen, followed by 24 h treatment with scrambled Aβ or 1 μM $Aβ_{1-42}$ ± 50 μM ferric ammonium citrate (FAC). **J** ICP-MS analysis of intracellular ^{56}Fe content from IMG cells following 24 h treatment with DMSO or ebselen, and 24 h scrambled Aβ ± FAC or $Aβ_{1-42}$ ± FAC treatment. Two-way ANOVA, *p < 0.05, **p < 0.01, ***p < 0.001, ****p < 0.0001 effect of Aβ or FAC treatment. $^{\#}p < 0.05$, $^{\#\#}p < 0.01$, $^{\#\#\#}p < 0.001$, $^{\#\#\#\#}p < 0.0001$ effect of treatment x ebselen. *ns* not significant. Data show a representative experiment with the mean ± S.E.M of 3–4 technical replicates, and experiment was repeated three times. Statistical outliers were removed using the Grubb's test

of microglial *Slc11a2* knockdown on aspects of behavior and cognition.

First, to assess locomotor activity and control for anxiety-like behavior, mice were tested in elevated zero maze (EZ maze, 5 min), open field chambers (45 min), and one-trial spontaneous alternation Y-maze tests (6 min) and total distance traveled was measured in each. In females, control *APP/PS1* mice did not exhibit differences in baseline locomotor activity compared to control WT female mice in any of the assays tested (Fig. 3A–F; $p > 0.05$). However, microglial $Slc11a2^{KD}$ female *APP/PS1* animals exhibited a significant increase in distance traveled in all three activity measurement assays compared to their non-*APP/PS1* WT counterparts (Fig. 3A, C, E, F; activity measurements, EZ maze: *APP/PS1,* $F(1,38) = 9.28$, $p = 0.004$, *Interaction effect,* $F(1,38) = 12.29$, $p = 0.001$; open field: *Interaction,* $F(1,39) = 5.36$, $p = 0.03$; Y-maze activity: *APP/PS1,* $F(1,40) = 5.23$, $p = 0.03$, *Interaction,* $F(1,40) = 5.92$, $p = 0.02$; arm entries in Y-maze: *APP/PS1,* $F(1,40) = 5.76$, $p = 0.02$, *Interaction,* $F(1,40) = 7.93$, $p = 0.008$). As control measurements to assess for anxiety-like behavior, the amount of time spent in the open arms of the EZ maze (Fig. 3B, $p > 0.05$) or in the center area of the open field chambers were not significantly different (Fig. 3D, $p > 0.05$). Additionally, there were no significant differences in Y-maze spontaneous alternation capacity between any groups (Fig. 3G, $p > 0.05$).

Male *APP/PS1* mice exhibited a significant increase in activity in the EZ maze compared to WT controls (Fig. 4A; EZ Maze: *APP/PS1 effect,* $F(1,48) = 22.61$, $p < 0.0001$). There was a significant main effect of *Slc11a2* knockdown on activity in the EZ maze in males (*Knockdown effect,* $F(1,48) = 8.18$, $p = 0.0063$), and post-hoc analyses revealed that *Slc11a2* knockdown had a greater effect on the hyperactive phenotypes observed in the *APP/PS1* males compared to corresponding controls (Fig. 4A, EZ maze: Control vs. *APP/PS1,* $p = 0.013$, $Slc11a2^{KD}$ Control vs. $Slc11a2^{KD}$ *APP/PS1,* $p = 0.0006$). There were no differences in anxiety-like behavior in EZ maze (time spent in open arms, Fig. 4B). Male *APP/PS1* mice did not show any significant differences in total distance traveled or anxiety-like behavior in the open field chambers over 45 min (Fig. 4C, D, $p > 0.05$). However, there was a significant *APP/PS1*-associated increase in activity in a 6 min Y-maze in the males (Fig. 4E; Y-maze: *APP/PS1 effect,* $F(1,46) = 8.40$, $p = 0.006$), which was exacerbated in the *Slc11a2* knockdown animals (Fig. 4E, Y-maze activity post-hoc comparisons: Control vs. *APP/PS1,* $p = 0.39$, $Slc11a2^{KD}$ Control vs. $Slc11a2^{KD}$ *APP/PS1,* $p = 0.012$; Fig. 4F, Y-maze arm entries: $F(1,46) = 5.65$, $p = 0.02$; post-hoc comparisons: Control WT vs. *APP/PS1,* $p = 0.61$, $Slc11a2^{KD}$ WT vs. $Slc11a2^{KD}$ *APP/PS1,* $p = 0.03$). There were no significant differences in Y-maze spontaneous alternation capacity as a measure of working memory (Fig. 4G). Overall, these data suggest that

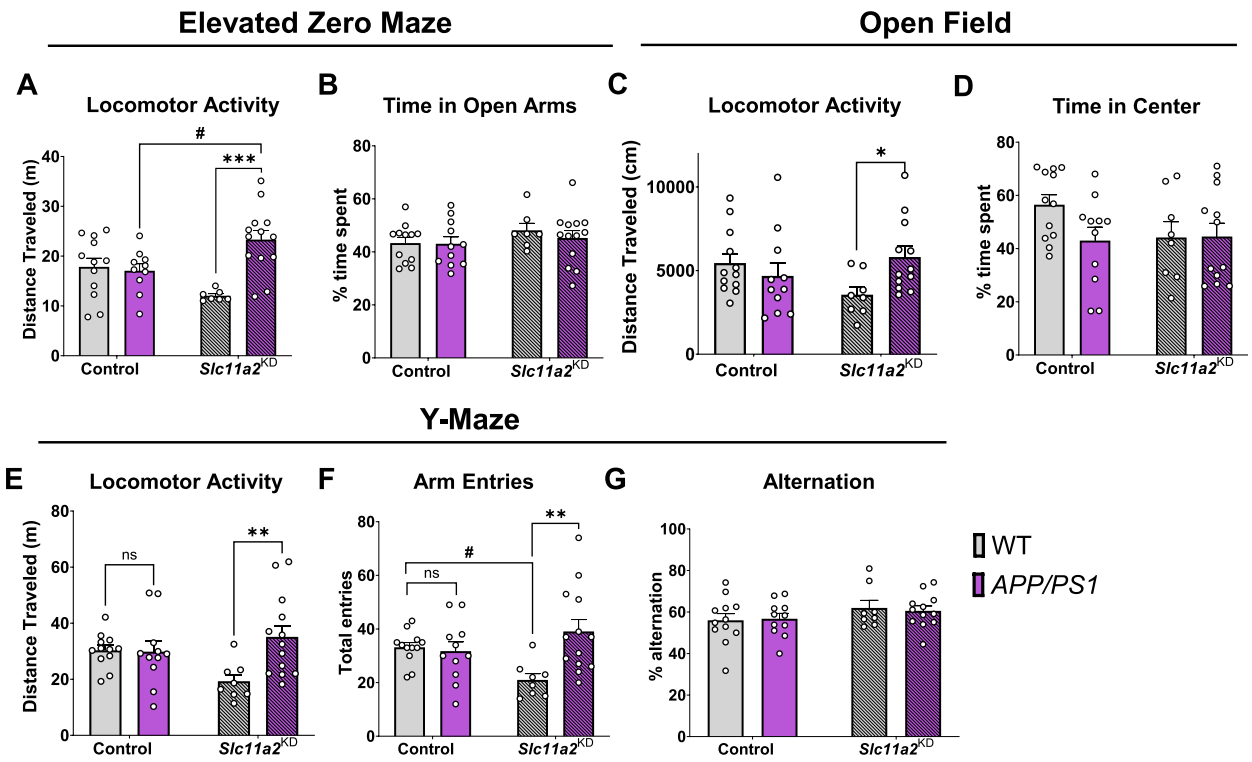

Fig. 3 Microglial *Slc11a2* knockdown results in a hyperactive phenotype in female *APP/PS1* mice at 12–15 months. **A**, **B** Elevated zero maze. **A** Total distance traveled (m) in control WT, control *APP/PS1*, *Slc11a2*^{KD} WT, and *Slc11a2*^{KD} *APP/PS1* female mice. **B** Total percent time spent in open arms. **C**, **D** Open field locomotor activity assay. **C** Total distance traveled (cm). **D** Total percent time spent in the center. **E**–**G** Exploratory Y-maze. **E** Total distance traveled (m). **F** Total number of different arm entries. **G** Total percent alternation. Two-way ANOVA, *p < 0.05, **p < 0.01, ***p < 0.001 effect of *APP/PS1* genotype, $^{\#}$p < 0.05 *Slc11a2*^{KD} vs. Control. *ns* not significant. Data represent the mean ± S.E.M of 8–13 female mice per group. Statistical outliers were removed using the Grubb's test

microglial *Slc11a2* knockdown is associated with an exaggerated hyperactive phenotype in the *APP/PS1* animals, particularly in female mice.

Slc11a2 knockdown worsens memory performance in Morris water maze and cued fear conditioning assay in *APP/PS1* females

To determine whether *Slc11a2* knockdown in vivo affects measurements of well-being, cognition, and longer-term learning and memory, several behavioral tasks were utilized. An overnight nest building assay revealed a robust *APP/PS1*-associated deficit in nestlet amount shredded in the females; however, there was no additional effect of *Slc11a2* knockdown on this measurement of cognition and well-being (Additional File 5A**;** Control WT mean, 4.3 g ± 0.28; Control *APP/PS1* mean, 1.73 g ± 0.30; *Slc11a2*^{KD} WT mean, 3.5 g ± 0.47; *Slc11a2*^{KD} *APP/PS1* mean, 1.48 g ± 0.35; *APP/PS1 effect,* $F(1,38) = 43.54$, $p < 0.0001$). To assess learning and spatial memory, mice underwent 5 days of trials to find a hidden platform in Morris water maze (MWM), a widely used test for hippocampal-dependent spatial navigation and memory. Over the course of 5 days, all female mice (regardless of *APP/PS1* genotype or *Slc11a2* knockdown) effectively learned the location of the platform compared to their baseline on day one, exhibiting significantly shorter latencies and path lengths to find the platform by day five (latencies in Additional File 5B; *Day effect,* $F(2.84, 113.5) = 8.05$, $p < 0.0001$; path length in Fig. 5A; *Day effect,* $F(2.75, 110.1) = 11.38$, $p < 0.0001$). Average swim speed during a 60 s probe trial was assessed as a control measure. Female *Slc11a2*^{KD} *APP/PS1* mice exhibited significantly greater swim speeds in the water maze compared to all other groups (Fig. 5B; *Knockdown x APP/PS1 Interaction,* $F(1,40) = 5.45$, $p = 0.025$). Because of the differences in swim speed, which may confound data reporting latency to find platform, path lengths to platform were measured. Female *APP/PS1* mice were not different than control WT females at finding the hidden platform during training days. However, microglial *Slc11a2*^{KD} female *APP/PS1* animals exhibited slightly longer path lengths to find the hidden platform, although this was not statistically significant (Fig. 5A**;** $p = 0.1$). Mice underwent one 60 s probe trial for memory of platform location

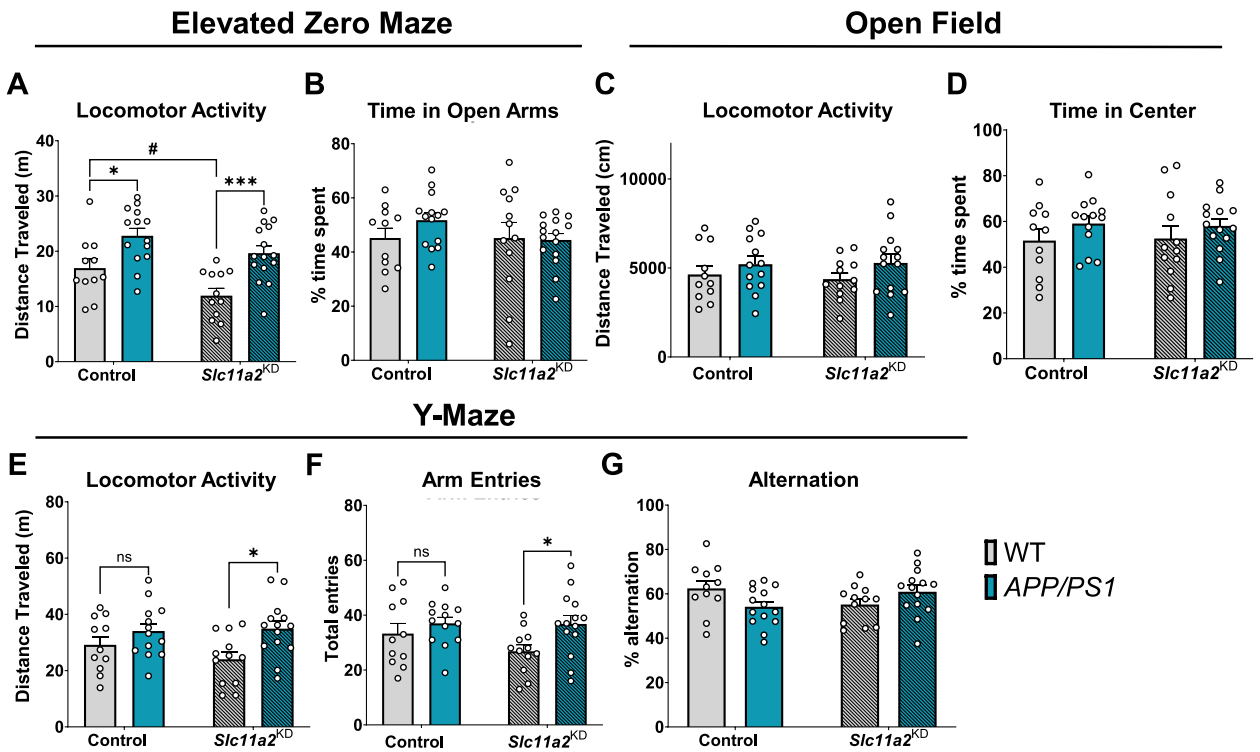

Fig. 4 Microglial *Slc11a2* knockdown worsens hyperactivity in a novel environment in male *APP/PS1* mice at 12–15 months. **A-B** Elevated zero maze. **A** Total distance traveled (m) in control WT, control *APP/PS1*, *Slc11a2*^{KD} WT, and *Slc11a2*^{KD} *APP/PS1* male mice. **B** Total percent time spent in open arms. **C**, **D** Open field locomotor activity assay. **C** Total distance traveled (cm). **D** Total percent time spent in the center. **E**–**G** Exploratory Y-maze. **E** Total distance traveled (m). **F** Total number of different arm entries. **G** Total percent alternation. Two-way ANOVA, *$p < 0.05$, ***$p < 0.001$ effect of *APP/PS1* genotype. $^{\#}p < 0.05$ *Slc11a2*^{KD} vs. Control. *ns* not significant. Data represent the mean ± S.E.M of 11–15 male mice per group. Statistical outliers were removed using the Grubb's test

24 h after the last set of training trials, in which the platform was removed from the pool and mice were allowed to swim freely. There were no significant differences in time spent in the target quadrant where the platform location was previously (Fig. 5C, $p > 0.05$); however, female *APP/PS1* mice overall exhibited a decrease in time spent around the exact platform location (exact platform location, plus 1.5 cm surrounding radius) compared to WT littermate controls (Fig. 5D; Females: *APP/PS1 effect,* $F(1,39) = 8.90$, $p = 0.005$). Female *Slc11a2*^{KD} *APP/PS1* mice exhibited a significant further reduction in time spent around the platform location, suggesting an exacerbated loss of memory function in these animals (Females: post hoc *analysis:* Control WT vs. Control *APP/PS1,* $p = 0.68$; *Slc11a2*^{KD} WT vs. *Slc11a2*^{KD} *APP/PS1,* $p = 0.004$). To further assess the effects of *Slc11a2* knockdown on memory function, we utilized a fear conditioning assay in which a tone was succeeded by a mild foot shock. During the initial training session, all groups significantly increased freezing by the third tone presentation, albeit *APP/PS1* females overall froze less over the course of the 8 min training session (Fig. 5E, *Time effect,* $F(6.9, 279.3) = 41.1$, $p < 0.0001$; *Interaction of Time x APP/PS1,* $F(15,600) = 4.91$, $p < 0.0001$). In the contextual fear conditioning assay, female *APP/PS1* mice exhibited a disease model-associated deficit in fear memory (Fig. 5F, *APP/PS1 effect,* $F(1,39) = 12.26$, $p = 0.0012$); although, there was no additional effect of *Slc11a2* knockdown. However, in the cued fear conditioning memory task, female *Slc11a2*^{KD} *APP/PS1* mice displayed a significant worsening in fear memory associated with presentation of a tone (Fig. 5G, *Knockdown x APP/PS1 Interaction,* $F(1,39) = 4.19$, $p = 0.047$). Indeed, although all females exhibited an increase in freezing in response to the presentation of the tone (*Tone,* $F(1,39) = 145.2$, $p < 0.0001$), female *Slc11a2*^{KD} *APP/PS1* mice were significantly less responsive compared to all other groups (Fig. 5H; *Interaction of Knockdown x APP/PS1,* $F(1,39) = 5.39$, $p = 0.026$).

Male *APP/PS1* animals displayed a significant deficit in nest building capacity compared to littermate WT control mice, with no additional effect due to *Slc11a2*^{KD} (Additional File 5C; Control WT mean, 3.17 g ± 0.52; Control *APP/PS1* mean, 2.03 g ± 0.41; *Slc11a2*^{KD} WT mean, 3.82 g ± 0.34; *Slc11a2*^{KD} *APP/PS1* mean,

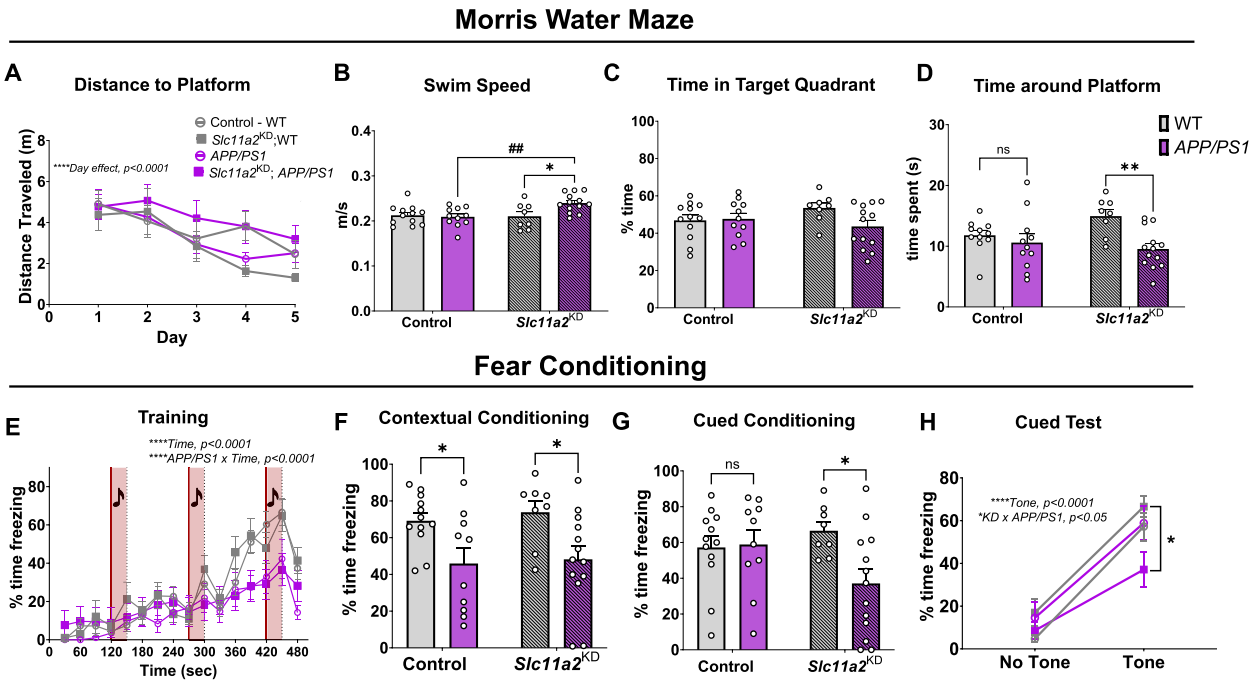

Fig. 5 Microglial *Slc11a2* knockdown worsens memory performance in Morris water maze and cued fear conditioning assay in *APP/PS1* female mice. **A**–**D** Morris water maze (MWM). **A** Total distance traveled (m) before reaching hidden platform over course of five training days in control WT, control *APP/PS1*, *Slc11a2*^{KD} WT, and *Slc11a2*^{KD} *APP/PS1* female mice. Four trials of 60 s each were conducted each day and averaged per animal. Three-way ANOVA, ****$p < 0.0001$ effect of day. **B** Average speed (m/s) measured during probe trial. Two-way ANOVA, *$p < 0.05$ effect of *APP/PS1* genotype. ##$p < 0.01$ *Slc11a2*^{KD} vs. Control. **C** Total percent time spent in the target quadrant in probe trial for memory. **D** Total time (s) spent around where the platform previously was (exact platform location + 1.5 cm radius) during probe trial for memory. **E**–**H** Fear conditioning assay. **E** Percent component time freezing during the 8 min training protocol. Every 2 min, a 30 s tone was played, followed by a mild foot shock. Increased freezing behavior over the course of the assay is shown. ****$p < 0.0001$ effect of time, ****$p < 0.0001$ effect of *APP/PS1* x time. **F** Percent time freezing during 4 min contextual fear conditioning test. **G** Total percent time spent freezing during the 4 min of cued fear conditioning testing. **H** Percent component time spent freezing during 2 min of no-tone versus 2 min of tone presentation in cued fear conditioning test. ****$p < 0.0001$ effect of tone, *$p < 0.05$ *Slc11a2*^{KD} *APP/PS1* vs. Control *APP/PS1*. Data represent the mean ± S.E.M. of 8–13 mice per group. Statistical outliers were removed using the Grubb's test

2.35 g ± 0.44; *APP/PS1 effect,* $F(1,47) = 9.15$, $p = 0.004$). In the MWM, all males regardless of experimental group learned the location of the platform by the end of five training days, albeit *APP/PS1* males exhibited longer latencies and path lengths over the course of the training compared to WT controls (latencies shown in Additional File 5D; *Day effect,* $F(3.08, 144.7) = 18.30$, $p < 0.0001$; *APP/PS1* effect, $F(1,47) = 7.84$, $p = 0.007$; *APP/PS1* x *Day,* $F(4,188) = 2.76$, $p = 0.029$; path lengths shown in Fig. 6A**;** Males: *Day effect,* $F(2.891, 135.9) = 20.45$, $p < 0.0001$; *APP/PS1* effect, $F(1, 47) = 5.99$, $p = 0.018$). This behavioral phenotype was observed in the absence of differences in swim speeds between groups (Fig. 6B, $p > 0.05$), demonstrating a disease model-associated learning deficit in the males. In the MWM probe trial, there were no significant differences between groups in time spent in the target quadrant of the previous platform location (Fig. 6C, $p > 0.05$); however, male *APP/PS1* mice overall spent significantly less time around the remembered platform location (platform location, including 1.5 cm surrounding radius) compared to WT controls (Fig. 6D; Males: *APP/PS1 effect,* $F(1,46) = 6.55$, $p = 0.01$). There were no differences in male *Slc11a2*^{KD} animals compared to *Slc11a2*-intact control animals in MWM. In the fear conditioning task, male *APP/PS1* animals exhibited decreased freezing during the training session (Fig. 6E, *Interaction of Time x APP/PS1,* $F(15, 705) = 2.25$, $p = 0.004$). There were no significant differences between any groups of the males in the contextual fear conditioning assay (Fig. 6F, $p > 0.05$), although male *APP/PS1* mice overall performed worse on the cued fear conditioning task for memory compared to WT controls (Fig. 6G, H, *APP/PS1 effect,* $F(1,46) = 4.15$, $p = 0.047$). *Slc11a2* knockdown had no effect on performance in these assays in the males. Overall, these data suggest that microglial *Slc11a2* knockdown is associated with significant worsening of cognitive dysfunction in several tasks in a sex-specific manner, particularly in female *APP/PS1* animals.

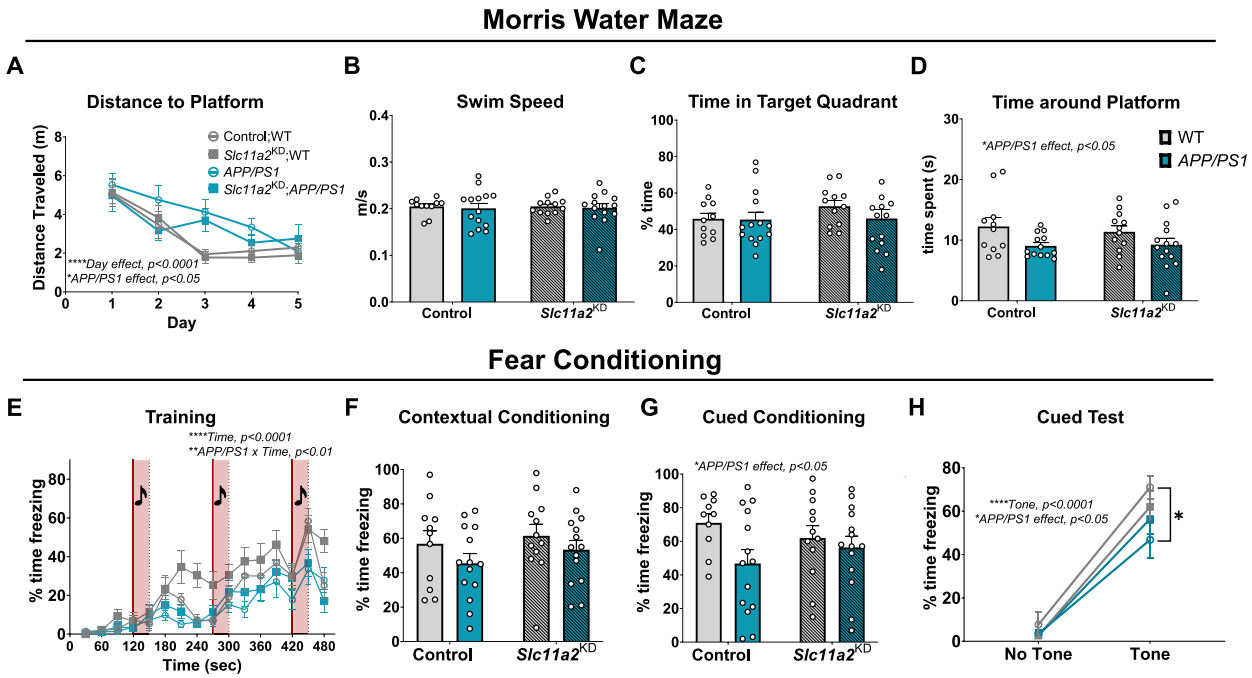

Fig. 6 Microglial *Slc11a2* knockdown has no effect on memory performance in male mice. **A-D** Morris water maze (MWM). **A** Total distance traveled (m) before reaching hidden platform over course of five training days in control WT, control *APP/PS1*, $Slc11a2^{KD}$ WT, and $Slc11a2^{KD}$ *APP/PS1* male mice. Four trials of 60 s each were conducted each day and averaged per animal. Three-way ANOVA, ****$p < 0.0001$ effect of day, *$p < 0.05$ effect of *APP/PS1*. **B** Average speed (m/s) measured during probe trial. Two-way ANOVA, *$p < 0.05$ effect of *APP/PS1* genotype. $^{\#\#}p < 0.01$ $Slc11a2^{KD}$ vs. Control. **C** Total percent time spent in the target quadrant in probe trial for memory. **D** Total time (s) spent around where the platform previously was (exact platform location + 1.5 cm radius) during probe trial for memory. **E**–**H** Fear conditioning assay. **E** Percent component time freezing during the 8 min training protocol. Every 2 min, a 30 s tone was played, followed by a mild foot shock. Increased freezing behavior over the course of the assay is shown. ****$p < 0.0001$ effect of time, **$p < 0.0001$ effect of *APP/PS1* x time. **F** Percent time freezing during 4 min contextual fear conditioning test. **G** Total percent time spent freezing during the 4 min of cued fear conditioning testing. **H** Percent component time spent freezing during 2 min of no-tone versus 2 min of tone presentation in cued fear conditioning test. *$p < 0.05$ effect of *APP/PS1* genotype, ****$p < 0.0001$ effect of tone. Data represent the mean ± S.E.M. of 11–14 mice per group. Statistical outliers were removed using the Grubb's test

Hippocampal microglia from female $Slc11a2^{KD}$ *APP/PS1* animals exhibit significant alterations in subsets of DAM-like inflammatory and oxidative genes

Significant alterations in gene expression from isolated microglia have been shown in AD models and human patients [35, 36]. Thus, to examine transcriptomic changes in *Slc11a2* knockdown microglia in our in vivo studies, we magnetically isolated $CD11b^{+}$ microglia from the bilateral hippocampus from female mice for bulk RNA-sequencing. We focused this RNA-seq analysis on the females to delve deeper into the molecular changes that may underlie the behavioral and memory-associated deficits we observed only in the female $Slc11a2^{KD}$ *APP/PS1* mice. In the *Slc11a2* knockdown microglia, we first confirmed abrogation of expression in the *Slc11a2* gene between exons 6–8 (Additional File 4**A**), similar to what has been shown by others in this mouse model used to knockdown *Slc11a2* [76, 77]. Principal component analysis revealed a primary effect of *APP/PS1* genotype on overall gene expression in isolated cells (Fig. 7A). As expected, hippocampal microglia isolated from *APP/PS1* control animals exhibited a significant and robust pattern of differential gene expression compared to microglia isolated from WT controls. We found 1236 differentially expressed genes (DEG) that were elevated in microglia from *APP/PS1* control animals and 1308 genes that were significantly downregulated in *APP/PS1* controls compared to WT controls (adjusted p-value < 0.05). In examining the top 50 DEG (by fold-change and adj. p-value) in hippocampal microglia isolated from *APP/PS1* compared to WT control females, we observed changes in similar gene markers previously reported in AD-associated microglia. Specifically, there were robust increases in microglial phagocytic marker *Cd68* [78], hypoxia-related gene *Hif1α* [79], aging-associated marker *Clec7a* [80], lipid-droplet-associated marker *Plin2* [81], as well as Type I IFN-signaling gene, *Mamdc2* [82] (Additional File 6A). DEGs that were downregulated in *APP/PS1* hippocampal microglia compared to WT controls included homeostatic microglial marker *Tmem119,* as well as

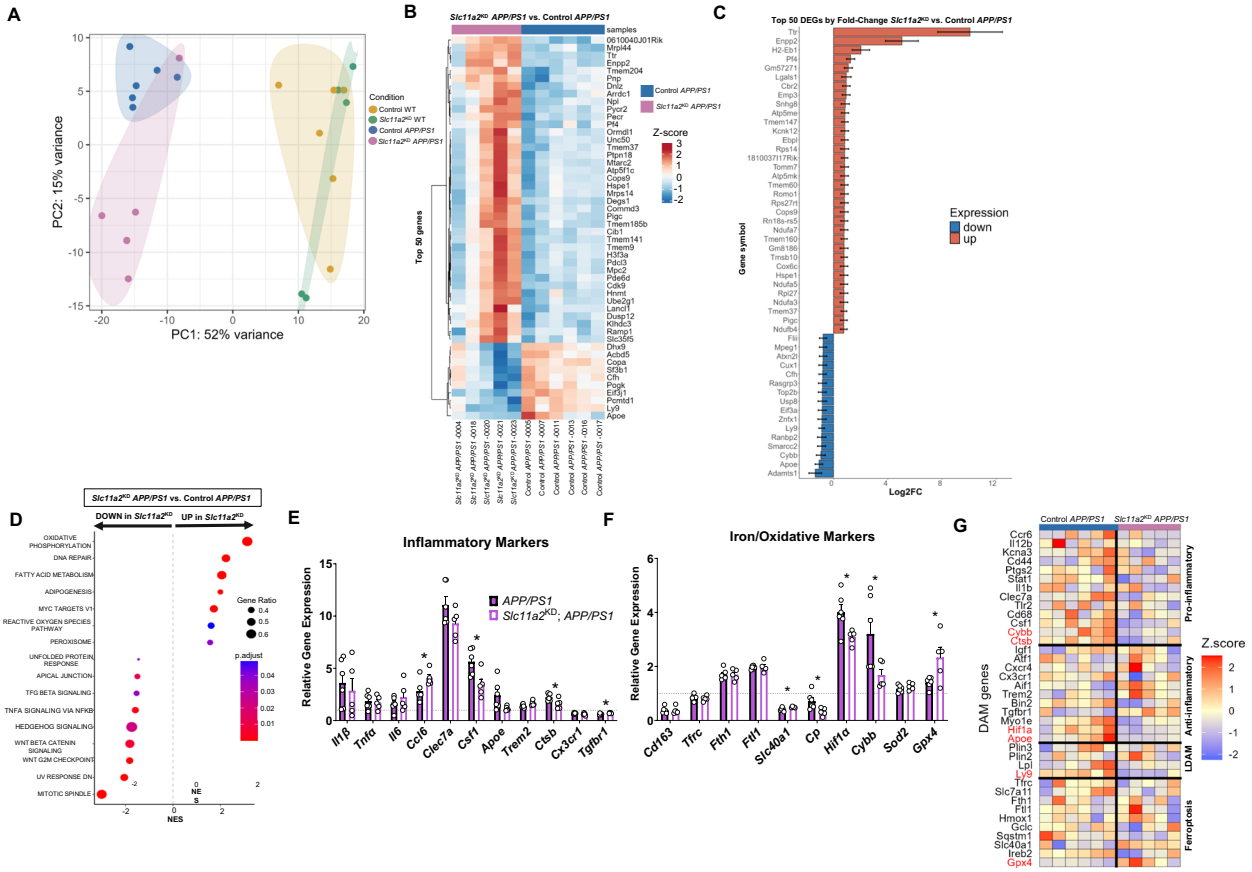

Fig. 7 *Slc11a2* knockdown shifts transcriptional profile and alters several DAM-related gene markers in hippocampal microglia from female *APP/PS1* mice. **A** Principal component analysis (PCA) of bulk RNA-seq gene expression in sorted CD11b^{+} microglia from control WT, control *APP/PS1*, *Slc11a2*^{KD} WT, and *Slc11a2*^{KD} *APP/PS1* mice. Primary differences in overall gene expression are a result of *APP/PS1* genotype. **B** Heat map of top 50 DEGs (by adjusted p-value in RNA-seq dataset) between *Slc11a2*^{KD} *APP/PS1* versus control *APP/PS1* microglia. Blue = downregulated in *Slc11a2*^{KD} cells, lighter blue and/or red = upregulated in *Slc11a2*^{KD} cells. **C** Top 50 DEGS by fold-change in RNA-seq analysis between *Slc11a2*^{KD} *APP/PS1* and control *APP/PS1* microglia. Red = upregulated in *Slc11a2*^{KD}, blue = downregulated in *Slc11a2*^{KD} cells. **D** GSEA analysis of hallmark gene pathways significantly altered between *Slc11a2*^{KD} *APP/PS1* and control *APP/PS1* microglia. **E**, **F** Relative gene expression of targeted **E** inflammatory markers and **F** iron and oxidative stress markers from *Slc11a2*^{KD} *APP/PS1* versus control *APP/PS1* microglia in the RNA-seq dataset. Gene expression is relative to control WT average (black dotted line set to 1). *$p < 0.05$, student's t-test comparing *Slc11a2*^{KD} *APP/PS1* vs. control *APP/PS1*. **G** Gene markers representing subsets of DAMs (i.e., pro-inflammatory, anti-inflammatory, LDAM, and ferroptosis) were analyzed via RNA-seq between Control and *Slc11a2*^{KD} *APP/PS1* female microglia. Genes highlighted in red are significantly different between groups, adjusted p-value < 0.05. Data represent the mean ± S.E.M. of 5–6 mice per group

iron export gene, *Slc40a1* (ferroportin) (Additional File 6B). Gene-set enrichment analysis (GSEA) revealed significant upregulations in genes involved in cholesterol homeostasis, cellular metabolism, and inflammatory activation in *APP/PS1* microglia (Additional File 6C), similar to what others have shown previously in AD models [83].

To determine the effect of *Slc11a2* knockdown on hippocampal microglia, we first compared microglial gene expression between *Slc11a2*^{KD} and Control WT females. As a result of knockdown alone, we only found 10 DEGs (Additional File 7A). Top genes altered included *Ccr6* and *Cd5* (Additional File 7B, C). We then aimed to determine how *Slc11a2* knockdown affects microglial gene expression in the *APP/PS1* female animals. There were 449 genes significantly upregulated and 130 downregulated in microglia isolated from *Slc11a2*^{KD} *APP/PS1* animals compared to microglia from control *APP/PS1* mice. Of these DEGs, *Enpp2* and *Ttr* were robustly upregulated in knockdown cells compared to controls (Fig. 7B). Of the top 50 identified DEGs between *Slc11a2*^{KD} *APP/PS1* and control *APP/PS1* females, *Apoe* (encoding apolipoprotein E), *Cybb* (gene for NOX2), and lipid-droplet-accumulating microglia (LDAM) marker, *Ly9,* were also significantly downregulated in the knockdown cells compared to the control *APP/PS1* cells (Fig. 7B, C). GSEA in the *Slc11a2*^{KD} and control *APP/PS1* microglia revealed

significant increases in genes associated with cellular metabolism—in particular, oxidative phosphorylation and fatty acid metabolism—and reactive oxygen species (ROS) pathways (Fig. 7D). *Slc11a2* knockdown cells also exhibited significant decreases in genes associated with TNF and NFκB inflammatory signaling and Wnt signaling, as indicated by gene-set enrichment pathway analysis (Fig. 7D). When comparing relative expression of specific genes in the sequencing dataset, we observed significant alterations in several genes involved in inflammatory and oxidative stress-associated pathways in *Slc11a2*^{KD} versus control cells from *APP/PS1* females. Specifically, we observed a significant decrease in *Ctsb* and *Csf1* (markers associated with DAMs) [84] in the knockdown cells, as well as a significant increase in *Tgfbr1* ($p < 0.05$) and increase in *Trem2* compared to control cells (although not statistically significant, $p = 0.068$) (Fig. 7E). In examining genes related to iron handling and redox status, we observed a significant increase in iron exporter gene *Slc40a1* and antioxidant gene *Gpx4* in *Slc11a2*^{KD} *APP/PS1* cells compared to control *APP/PS1* microglia (Fig. 7F). Additionally, *Slc11a2* knockdown cells exhibited decreases in pro-oxidant genes, such as *Hif1α* and *Cybb*, and a robust decrease in the iron-related gene encoding ceruloplasmin (*Cp*) (Fig. 7F). To assess changes in specific DAM-like markers further, we conducted targeted analysis of gene sets related to different subsets of DAMs reported in the literature [36, 85–88], including a 'pro-inflammatory', 'anti-inflammatory', 'lipid-associated DAM (LDAM)', and 'ferroptosis' gene set (Fig. 7G). These data further demonstrate that *Slc11a2* knockdown resulted in changes to some, but not all, DAM markers. Although *Slc11a2*^{KD} cells isolated from *APP/PS1* mice exhibited significant differences in the expression of several markers compared to control *APP/PS1* microglia, *Slc11a2*^{KD} *APP/PS1* microglia displayed a transcriptional profile still distinct from control, non-*APP/PS1* WT cells (black dotted line, Fig. 7E, F). In comparison to control WT cells, *Slc11a2*^{KD} *APP/PS1* microglia upregulated DAM and aging-related markers *Csf1, Hif1α, Cybb,* and *Ctsb*—albeit, to a lesser degree than control *APP/PS1* microglia.

Initial assessment of overall gene expression via PCA and DEGs in these samples revealed significant variance in gene expression in one sample in the *Slc11a2*^{KD} *APP/PS1* group compared to the rest of the *Slc11a2*^{KD} *APP/PS1* biological replicates (sample labeled as -0004 in PCA plot shown in Additional File 4B and in heat map Fig. 7B). Although this sample was not considered to be a statistical outlier, further RNA-seq analyses conducted following the removal of this sample are shown in Additional File 8. In this analysis, there were 2230 genes significantly upregulated and 2210 significantly downregulated in the *Slc11a2*^{KD} versus control *APP/PS1* females (Additional File 8B). The top DEGs revealed upregulations in genes including phagocytic-associated *Igkc,* along with *Ttr* and *Enpp2,* and prostaglandin-signaling molecule, *Ptgds* (Additional File 8C and D). *Slc11a2*^{KD} cells also exhibited significant downregulations in several DAM markers—particularly from the 'pro-inflammatory' gene subset—including *Cybb, Stat1,* and *Ctsb,* as well as *Ly9, Hif1α,* homeostatic marker *Bin2,* and *Apoe* (Additional File 8G). Overall, these data suggest that microglial *Slc11a2* knockdown in females decreases expression of some markers related to subsets of DAMs and aged cells in the *APP/PS1* model. Several DEGs found in female *Slc11a2* knockdown microglia were probed via RT-qPCR in male hippocampal microglia and are shown in Additional File 9. There were no significant changes in *Hif1α, Cybb,* or *Il1β* in male microglia due to *Slc11a2* knockdown, mirroring the lack of behavioral differences in the male *Slc11a2*^{KD} mice.

Discussion

Iron-loaded microglia are a hallmark of several neurodegenerative diseases, including AD [89–91]. Reactive microglia surrounding Aβ plaques exhibit a significant upregulation of ferritin-L (*Ftl1*) across AD mouse models and human patients and is a defining feature of DAMs across multiple disease models [31, 35, 36, 92]. Furthermore, recent in vitro work showed that iron loading specifically in microglia underlies subsequent neurotoxicity and cell death, positioning microglial iron load as a central mediator of neurodegeneration [29]. Inflammatory signals and iron import mechanisms are intimately connected ([20, 24], our data also in IMG cells). Increased iron levels have been shown to enhance pro-inflammatory cytokine secretion [45], toxic ROS production [40], and cellular senescence and dysfunction [75, 93]. Reciprocally, AD-associated inflammatory stimuli such as Aβ and bacterial lipopolysaccharide (LPS) upregulate the iron importer DMT1 in microglia.

In our studies in primary microglia from aged and young mice treated in vitro with pro-inflammatory oligomeric $A\beta_{1\text{-}42}$, we observed that the Aβ-induced increase in *Slc11a2* was exacerbated in microglia from aged compared to young mice. This age-associated increase in *Slc11a2* expression was accompanied by a significant upregulation in iron storage genes *Ftl1* and *Fth1* and augmented Aβ-induced inflammatory markers, suggesting a primed cellular state [94, 95]. These findings demonstrate an association between augmented Aβ-induced inflammation and iron loading markers in aged cells and implicate a synergy between age and Aβ leading to increased microglial *Slc11a2* expression. It may be that DMT1/*Slc11a2* plays a role in mediating the cellular

iron and inflammatory load observed in neurodegenerative disease. Indeed, a role for DMT1 in Parkinson's disease is well-appreciated [96, 97]. However, no studies to our knowledge have examined whether altering microglial DMT1/*Slc11a2* in vivo affects the development of chronic inflammation and disease-associated hallmarks in AD.

To investigate the effects of cell-specific alteration of *Slc11a2* in AD, we generated a novel model of tamoxifen-inducible, microglial-specific knockdown of *Slc11a2* in the *APP/PS1* mouse model of AD. In female *Slc11a2*^{KD} *APP/PS1* mice, we observed a significant worsening of behavioral phenotypes and cognitive performance at 12–15 months of age. Specifically, female *Slc11a2*^{KD} *APP/PS1* animals were significantly more hyperactive than all other female groups in multiple assays conducted. Previous studies have presented conflicting data on hyperactivity in AD mouse models, depending on the age and AD model used [98–100]. Our data showing hyperactivity in female *Slc11a2*^{KD} *APP/PS1* mice and male control *APP/PS1* mice at 12–15 months replicate data from others, who have shown significant hyperactivity in mouse models of AD at both early and later stages [98, 101–103]. Additionally, AD human patients often exhibit disruptions in psychiatric behaviors such as hyperactivity, impulsivity, and disinhibition [104]. While work is ongoing to elucidate the mechanisms driving hyperlocomotion in these animals, others have demonstrated increased neuronal excitability and calcium transients during exploratory behavior in AD model mice [105]. It may be that microglial *Slc11a2* knockdown affects microglial-neuronal interactions and leads to alterations in neuronal function that drive this hyperactive behavior. Further work is warranted to understand the mechanisms driving hyperactivity in AD models. Aside from the hyperactivity observed in Y-maze, we note that the lack of difference between WT and *APP/PS1* mice in working memory capacity in this task was unexpected. Previous work has also reported no difference in baseline spatial working memory between WT and *APP/PS1* mice in a Y-maze task [106, 107], and our conflicting results, as theirs, may in part be due to age and strain of mice tested, AD model characteristics, stress level of the mice, and/or apparatus design.

To assay for changes in memory function utilizing a more sensitive task, we utilized the MWM test [58, 108]. *Slc11a2* knockdown resulted in a significant worsening of memory function in *APP/PS1* females in the MWM memory probe trial. To further probe this memory phenotype, we used a fear conditioning assay consisting of both a contextual conditioning and cued conditioning task. We observed a significant deficit in learned cued fear memory in female *Slc11a2*^{KD} *APP/PS1* mice compared to control WT and *APP/PS1* mice. The cued fear conditioning task utilizes the re-presentation of a cue (a tone previously paired with a shock) and requires the use of separate, parallel neural processing systems from the contextual fear memory task. These involve inputs from the amygdala, insular cortex, regions in the parietal and temporal lobes, sensory cortices, and thalamus [109, 110]. These complex networks likely converge with hippocampal circuits to acquire and express fear memory associated with a conditioned stimulus [111]. Interestingly, dysfunction and neurodegeneration in the amygdala [112–114] and insular cortex [115, 116] have been implicated in AD models and patients as an early indicator of disease, and may also underlie many of the neuropsychiatric symptoms observed, such as hyperactivity and agitation [117]. The deficits we observed in cued fear memory in the female *Slc11a2*^{KD} *APP/PS1* mice, paired with their significant hyperactivity, suggest that *Slc11a2* knockdown may worsen AD-associated behavior mediated by both hippocampal and non-hippocampal-dependent circuits. These data thus reflect a sex-specific, disease-modifying cognitive effect of *Slc11a2* knockdown in female, but not male, *APP/PS1* mice.

The sex-differential effects of microglial *Slc11a2* knockdown are of particular interest in relation to AD development. In humans, females are significantly more likely to develop AD than males [118, 119], and female mice display enhanced pathological hallmarks compared to males in AD models [120–123]. In the studies reported here, we observed effects of microglial *Slc11a2* knockdown in female, but not male, *APP/PS1* mice, suggesting a potential pathway involved in worsening disease parameters in female mice. Sex differences in brain iron-handling and changes in iron-associated markers related to disease development are not well understood. In humans, brain ferritin levels are generally higher in older males than females in several regions [124], which is thought to contribute to the risk for males developing neurodegenerative disease at comparatively earlier ages [125]. In females, but not males, iron-deficiency anemia is associated with the development of dementia [126]. On the other hand, there is a significant rise in serum ferritin levels associated with menopause in aging females [127] that has been directly correlated with declining cognitive performance [128]. In mice, males have higher brain iron levels than females [129], and adult male and female mice differentially alter brain iron stores in iron-deficient conditions [130]. Additionally, research has illuminated significant sex differences in microglial morphology, inflammatory markers, and activity in age and disease, which may also contribute to sex differences in AD development [131, 132]. While work is ongoing to determine the mechanisms driving these sex differences,

sex steroid hormone exposure during critical periods of development is thought to be a primary driver of immune cell sex differences [133, 134]. Additionally, epigenetic mechanisms such as differences in DNA methylation and histone modifications have been posited to play key roles in driving sex differences in immune cell reactivity and function [131]. Future experiments utilizing gonadectomized rodents could further elucidate whether gonadal hormones per se are primary drivers of the sex differences we observed. Although the exact associations between brain iron status, sex, and microglial function are still being elucidated, our work suggests that a microglial inflammatory-iron-related pathway is relevant to sex-dependent differences in inflammation and disease progression.

Although technical limitations confined us to gene expression analyses in these studies, we note that future work aimed at quantifying DMT1 protein levels and cellular iron load in the *Slc11a2*^{KD} cells would be needed to expand upon these findings. While we cannot make definitive conclusions related to iron levels and/or protein-level changes in DMT1 and inflammatory makers per se, others have demonstrated an important role for transcriptional changes in inflammatory and iron-related genes [135, 136]. Indeed, the association between *Slc11a2* knockdown, changes in behavioral function, and alterations in expression of other genes is compelling to suggest a role for *Slc11a2* in mediating disease-associated processes. Furthermore, many studies have characterized the microglial transcriptional landscape during AD [80, 86, 137]. We conducted RNA-seq on isolated hippocampal microglia from the female mice to assess transcriptional changes that may underlie the cognitive differences observed. We found robust increases in *Enpp2,* or ectonucleotide pyrophosphatase 2, and *Ttr,* the gene encoding for transthyretin, in *Slc11a2*^{KD} *APP/PS1* microglia compared to controls. Although there is a possibility these genes are associated with choroid plexus contamination in the hippocampal samples [138, 139], previous work in neuroinflammation and AD models has identified downregulations in these genes in specific DAM subsets [140–142]. These two genes play roles in protein folding, Aβ binding, and lipid signaling, and have been suggested to play significant deleterious roles in microglia during aging and disease, when they are increased [143, 144].

Slc11a2^{KD} cells from *APP/PS1* females also exhibited decreases in subsets of DAM-like and age-associated markers, such as *Apoe, Ly9, Csf1, Cybb, Hif1α, Nfe2l2,* and *Ctsb.* Upregulations in these genes in AD-associated microglia are thought to represent a 'primed' microglial expression state initiated in response to mounting pathology and may help limit excessive oxidative damage in disease [35, 36, 142, 145–148]. Thus, decreases in these markers in the *Slc11a2*^{KD} cells may reflect the loss of a protective transcriptional state. *Slc11a2*^{KD} cells from *APP/PS1* females also displayed a decrease in *Bin2,* a marker related to cell migration and phagocytosis. Others have suggested that a decrease in *Bin2* promotes a deleterious transition in microglia during AD progression [146, 149]. Our data thus suggest that *Slc11a2* knockdown in microglia during AD progression leads to decreased expression of 'protective' DAM-like markers associated with limiting cellular damage, and instead an exacerbation of deleterious changes observed in aged and AD-associated microglia. Indeed, this may underlie the unexpected behavioral results observed. Our original hypothesis was that inhibiting *Slc11a2* would improve behavior and cognition based on our previous work showing an association between decreased inflammatory markers and improved sickness behavior in our acute LPS model [42]. However, data presented here suggest that decreased expression of several of these disease-associated microglial markers instead worsened disease parameters. It may be that these inflammatory and pro-oxidant pathways in microglia are important for protecting neural function during long-term chronic disease.

With the exception of differences in iron export gene, *Slc40a1,* and ceruloplasmin gene, *Cp,* there were few significant changes in iron-associated genes in *Slc11a2*^{KD} cells in our RNA-seq data. This could suggest that the effect of *Slc11a2* knockdown is primarily on select DAM-related markers and not on iron markers per se, or it could reflect a time-dependent transcriptional change in those markers during AD progression that was not captured at the time point tested. Our in vitro work demonstrated that ebselen robustly decreases Aβ-induced inflammatory markers and decreases iron load. Ebselen functions as a potent DMT1 inhibitor [63] and is also a peroxidase mimetic, and thus holds potential as a therapeutic to limit cellular iron uptake, ROS production, and inflammatory signaling [150–152]. Indeed, ebselen can improve phenotypes in AD models, and this may be due in part to its effects exerted on DMT1 and iron-handling [153, 154]. While our in vivo work cannot definitively demonstrate that the effects of DMT1 knockdown are due to differences in iron load per se, it is intriguing to note that the directional changes in subsets of inflammatory and oxidative markers in microglia from the *Slc11a2*^{KD} females are in the same direction as the anti-inflammatory and antioxidant effects of ebselen. Indeed, our pathway analysis in the RNA-seq dataset revealed decreases in TNF signaling, mimicking the in vitro findings that *Slc11a2* knockdown decreases inflammatory markers. Future work is needed to measure levels of iron in knockdown cells to conclusively determine the cellular

effects of knockdown. However, even if total cellular iron levels do not change due to *Slc11a2* knockdown, it could be that alterations in DMT1 affect the localization or distribution of iron in the cell that then alters inflammatory signaling. A difference in cellular iron distribution can lead to altered free radical production, which has been shown to directly affect inflammatory signaling pathways via modulation of NFκb signaling [155–158]. Future studies are needed to examine the mechanism by which these alterations in DMT1 and inflammatory signaling affect microglial function, as well as the mechanisms by which Aβ drives DMT1 expression. Future studies could also examine Aβ clearance capacity, as microglia play critical roles in plaque clearance in vivo [159]. Co-cultures with other cells (i.e., neurons) would also help elucidate how these differences in microglial inflammatory signaling affect overall neural function in disease.

Overall, it is intriguing to consider how the findings at the cellular level relate to the changes we observed in disease progression in vivo. Our initial hypothesis was that knocking down *Slc11a2* would improve cognition, based on decreases in microglial inflammation and iron load. Although we observed decreases in some cellular inflammatory markers, as hypothesized, these changes instead correlated with deficits in several behavioral tasks in female mice. This work thus adds to the growing body of data pointing to the nuanced role for microglial function and inflammation during disease. It may be that microglial increases in iron-related markers and inflammation are initially a neuroprotective measure, whereas a late transition to an iron-import phenotype exceeds the cell's capacity for non-toxic iron-handling and leads to neurodegenerative consequences [29, 160].

Conclusions

In conclusion, this work highlights a sex-specific effect of microglial knockdown of iron import gene *Slc11a2* on behavior and cognitive function in the *APP/PS1* mouse model of AD. Female *Slc11a2*^{KD} *APP/PS1* mice are significantly more hyperactive and display worsened memory phenotypes compared to control animals. Associated with these behavioral changes, microglia from *Slc11a2*^{KD} *APP/PS1* females display a transcriptional shift demonstrating decreased DAM-like markers purported to be protective. These data suggest that microglial knockdown of iron import gene, *Slc11a2,* leads to a progressive worsening of disease parameters in female AD mice and illuminate a microglial inflammatory-iron-associated pathway that holds relevance to our understanding of the complex roles of iron and microglia in neurodegenerative disease.

Abbreviations

Aβ	Amyloid-beta
AD	Alzheimer's disease
Apoe	Apolipoprotein E
APP/PS1	APPswe,PSEN1dE9
CNS	Central nervous system
DAM	Disease-associated microglia
DEG	Differentially expressed genes
DMSO	Dimethyl sulfoxide
DMT1	Divalent metal transporter 1
EZM	Elevated zero maze
FAC	Ferric ammonium citrate
Fth	Ferritin heavy chain
Ftl	Ferritin light chain
GSEA	Gene set enrichment analysis
Hif1α	Hypoxia-inducible factor 1 α
ICP-MS	Inductively-coupled plasma mass spectrometry
IL	Interleukin
IMG	Immortalized microglial cell line
KD	Knockdown
MWM	Morris water maze
PCA	Principal component analysis
ROS	Reactive oxygen species
Slc11a2	Solute carrier family 11 member 2
Tnfa	Tumor necrosis factor α
WT	Wild-type

Supplementary Information

The online version contains supplementary material available at https://doi.org/10.1186/s12974-024-03238-w.

Additional file 1. Experimental model and timeline diagram. A Schematic of mouse model generated in these studies. *Slc11a2*$^{fl/fl}$;*Cx3cr1*$^{Cre\text{-}ERT2+/+}$ mice were bred with *Slc11a2*$^{fl/fl}$;*APP/PS1*$^{+}$ hemizygotes to yield two resultant genotypes: *Slc11a2*$^{fl/fl}$;*Cx3cr1*$^{Cre\text{-}ERT2+/-}$;*APP/PS1*$^{+}$ and *Slc11a2*$^{fl/fl}$;*Cx3cr1*$^{Cre\text{-}ERT2+/-}$;WT. Tamoxifen was administered to half the animals to induce knockdown of microglial *Slc11a2*, and corn oil was used as a control. This resulted in four experimental groups: Control WT, *Slc11a2*^{KD} WT, Control *APP/PS1*$^{+}$, and *Slc11a2*^{KD} *APP/PS1*$^{+}$. B Timeline of experiments. Tamoxifen gavage was used to induce *Slc11a2* knockdown at 5-6 months of age, and behavioral analyses were conducted between 12-15 months of age. Tissue was collected when mice were 15-18 months of age. C CD11b+ microglial cells were isolated from whole brains, and confirmation of *Slc11a2* knockdown was done via RT-qPCR using a primer targeting exons 7-8 in both sexes. Two-way ANOVA, ****p<0.0001 effect of knockdown.

Additional file 2. Mouse numbers and weights used in experiments. Supplemental Table 1 Mouse numbers used for behavioral assays. Supplemental Table 2 Body weights were assessed at time of euthanasia when mice were 15-18 months old. The data are presented as average weight in grams ± S.E.M. for 8–14 mice per group. One mouse from the male *Slc11a2*^{KD};*APP/PS1* group and one female Control *APP/PS1* mouse died prior to euthanasia.

Additional file 3. Antibodies and primers used. Supplemental Table List of antibodies used in immunofluorescent staining of isolated glia, and list of gene primers used for RT-qPCR

Additional file 4. Knockdown confirmation and outlier analysis in female microglia from RNA-seq. A RNA-seq read coverage across annotated exons in the *Slc11a2* gene using the package, ggcoverage v1.3.0. *Slc11a2*^{KD} samples exhibited complete abrogation of reads between exons 6-8. Sample ID numbers shown on right of plot. B PCA plot showing all samples in RNA-seq analysis. The red arrow is pointing to sample #10 in control *APP/PS1* group. C Outlier analysis of control *APP/PS1* group, showing #10 as statistical outlier. Data represent 5-7 mice per group.

Additional file 5. *Slc11a2* knockdown had no additional effect on *APP/PS1*-associated deficits in nest building or Morris water maze latency. A and C Amount nestlet shredded after overnight nest building assay. Two-way ANOVA, *p<0.05, **p<0.01, ***p<0.001, ****p<0.0001. B and D Latencyto reach hidden platform of Morris water maze during training days. Four trials per day were averaged for one data point per animal, and these

trials were repeated for five days. Three-way ANOVA, *p<0.05, **p<0.01, ****p<0.0001. Data represent the mean ± S.E.M. of 8-14 mice per group.

Additional file 6. Hippocampal microglia from female *APP/PS1* mice exhibit significant alterations in gene expression compared to WT. A Top 50 DEGS by adjusted p-value between *APP/PS1* and WT microglia. Heat map shows upregulations in *APP/PS1* cells in red and downregulations in blue. B Volcano plot showing genes differentially alteredin *APP/PS1* compared to WT microglia. C GSEA of significantly altered hallmark gene sets in *APP/PS1* cells compared to WT. Upregulated pathways in *APP/PS1* microglia include those involved in cholesterol homeostasis, inflammatory signaling, and metabolic changes. Data represent 5-6 mice per group.

Additional file 7. *Slc11a2*^{KD} microglia from WTfemale mice exhibit minimal alterations in gene expression compared to controls. A Number of DEGS from RNA-seq analysis comparing control WT and *Slc11a2*^{KD} WT groups. B Volcano plot showing genes differentially expressedin *Slc11a2*^{KD} versus control WT microglia. C Heat map showing top DEGSin *Slc11a2*^{KD} versus control WT microglia. Red = upregulated, blue = downregulated. Data represent 5-6 mice per group.

Additional file 8. Removal of variable sample from *Slc11a2*^{KD} *APP/PS1* group in RNA-seq data reveals robust effects of *Slc11a2*^{KD} on microglial gene expression in *APP/PS1* female mice. A–D Data from RNA-seq analysis when sample #4 is removed. A PCA plot showing separation of group clusters. B Number of DEGs between *Slc11a2*^{KD} and control *APP/PS1* microglia. C Heat map showing top 50 DEGSbetween *Slc11a2*^{KD} and control *APP/PS1* microglia. Red = upregulated, blue = downregulated. D Top 50 DEGs by log fold-change between *Slc11a2*^{KD} and control *APP/PS1* microglia. E, F Targeted gene expression analysis from RNA-seq dataset showing changes in E inflammatory markers and F iron-related and oxidative stress markers from *Slc11a2*^{KD} versus control *APP/PS1* microglia. Gene expression is shown relative to control WT group set to 1. *p<0.05, **p<0.01 student's t-test. G Gene markers representing subsets of DAMswere analyzed via RNA-seq between Control and *Slc11a2*^{KD} *APP/PS1* female microglia after removing sample #4. Genes highlighted in red are significantly different between groups, adjusted p-value < 0.05. Data represent mean ± S.E.M. of 4-6 mice per group.

Additional file 9. *Slc11a2* knockdown had no significant effect on *APP/PS1*-associated increases in *Hif1a, Cybb,* or *Il1β* in male hippocampal microglia. A-C) RT-qPCR gene expression analysis of A *Hif1a,* B *Cybb,* and C *Il1β* from isolated hippocampal CD11b+ microglia from male mice. Two-way ANOVA, **p<0.01, ****p<0.0001. Data represent the mean ± S.E.M. of 5-9 mice per group.

Acknowledgements
The authors would like to acknowledge Dr. Nathan Winn and Teri Doss for assistance with tamoxifen gavage. The authors thank Dr. Rich Breyer for providing the aged mice in the primary cell experiments. Behavioral experiments were conducted in the Murine Neurobehavior Core lab (MNL) at the Vanderbilt University Medical Center, and the authors would like to thank Dr. John Allison and Krista Paffenroth for technical training. The MNL receives support from the Vanderbilt Kennedy Center P50 HD103537. Bulk RNA-seq preparation, sequencing, and initial quality control analysis was performed in the Vanderbilt Technologies for Advanced Genomics (VANTAGE) core laboratory. VANTAGE is supported in part by Clinical and Translational Science Award Grant 5UL1 RR024975-03, Vanderbilt Ingram Cancer Center Grant P30 CA68485, Vanderbilt Vision Center Grant P30 EY08126, and National Institutes of Health/National Center for Research Resources Grant G20 RR030956. Additionally, RNA-seq data analysis in this work was performed by Creative Data Solutions, part of the Vanderbilt Center for Stem Cell Biology. RNA-seq processing leveraged the resources provided by the Vanderbilt Advanced Computing Center for Research and Education (ACCRE), a collaboratory operated by and for Vanderbilt faculty.

Author contributions
KVR designed the work and was responsible for study conception; designed and performed experiments; acquired, analyzed, and interpreted data; and prepared the manuscript. ASR performed experiments, acquired, and analyzed data; and revised the manuscript. JPC and SS analyzed and interpreted data and generated figures in the RNA-seq experiments; and revised the manuscript. MWS analyzed and interpreted data and generated figures from the RNA-seq dataset for the revised manuscript; and revised the manuscript. KRS and AMV performed, acquired, and analyzed data in the in vitro experiments; and revised the manuscript. ATK conducted additional RT-qPCR experiments and analyzed data; acquired data for the revised manuscript; and revised the manuscript. FEH and AHH designed the work; interpreted data; substantively revised the manuscript. All authors reviewed the results and approved the final version of the manuscript.

Funding
This project was funded by DK121520-02S1, a Pilot and Feasibility Award from the Vanderbilt Diabetes and Research Training Center (DK020593) and a Pilot and Feasibility Award from the Vanderbilt Memory and Alzheimer's Center (P20-AG068082) to AHH. AHH is also supported by a Career Scientist Award from the Veterans Affairs (IK6 BX005649). KVR was supported by the Molecular Endocrinology Training Program (T32 DK007563-31), the Interdisciplinary Alzheimer's Disease Training Program (T32-AG058524) and an individual Ruth L. Kirschstein National Research Service Award (1F31AG081025). MWS was supported by the Molecular Endocrinology Training Program (T32 DK007563-36). ATK is supported by NIEHS T32ES007028. FEH is supported by R01ES031401-05.

Availability of data and materials
The datasets supporting the conclusions of this article are available in the NCBI Gene Expression Omnibus (GEO) repository with accession ID GSE269314 (https://www.ncbi.nlm.nih.gov/geo/query/acc.cgi?acc=GSE269314). Other datasets used and/or analyzed are available from the corresponding authors on reasonable request. Additionally, sperm from *Slc11a2*$^{fl/fl}$; *Cx3cr1*$^{Cre\text{-}ERT2}$; *APP/PS1*$^{+}$ triple-transgenic male mice (129S;C57BL/6J) were cryopreserved at the Vanderbilt Genome Editing Resource to preserve the genetic line used in these studies, and are available for sharing upon request.

Declarations

Ethics approval and consent to participate
All studies using animals were approved by and conducted in compliance with the Institutional Animal Care and Use Committee (IACUC) at Vanderbilt University, protocol number #M2000113-00. No research was done with human participants, material, or data (Not applicable).

Consent for publication
Not applicable.

Competing interests
The authors declare no competing interests.

Author details
[1]Department of Molecular Physiology and Biophysics, Vanderbilt University, 702 Light Hall, Nashville, TN, USA. [2]Creative Data Solutions, Vanderbilt Center for Stem Cell Biology, Nashville, TN, USA. [3]Vanderbilt Brain Institute, Vanderbilt University, Nashville, TN, USA. [4]Department of Medicine, Vanderbilt University Medical Center, 7465 Medical Research Building IV, 2213 Garland Avenue, Nashville, TN 37232, USA. [5]VA Tennessee Valley Healthcare System, Nashville, TN, USA.

Received: 10 June 2024 Accepted: 19 September 2024
Published online: 27 September 2024

References

1. As A. 2023 Alzheimer's disease facts and figures. Alzheimers Dement. 2023;19(4):1598–695.
2. Kinney JW, Bemiller SM, Murtishaw AS, Leisgang AM, Salazar AM, Lamb BT. Inflammation as a central mechanism in Alzheimer's disease. Alzheimers Dement. 2018;4:575–90.

3. Cummings JL, Osse AML, Kinney JW. Alzheimer's disease: novel targets and investigational drugs for disease modification. Drugs. 2023;83(15):1387–408.
4. Belaidi AA, Bush AI. Iron neurochemistry in Alzheimer's disease and Parkinson's disease: targets for therapeutics. J Neurochem. 2016;139(Suppl 1):179–97.
5. Kenkhuis B, Bush AI, Ayton S. How iron can drive neurodegeneration. Trends Neurosci. 2023;46(5):333–5.
6. Liu JL, Fan YG, Yang ZS, Wang ZY, Guo C. Iron and Alzheimer's disease: from pathogenesis to therapeutic implications. Front Neurosci. 2018;12:632.
7. Sato T, Shapiro JS, Chang HC, Miller RA, Ardehali H. Aging is associated with increased brain iron through cortex-derived hepcidin expression. Elife. 2022. https://doi.org/10.7554/eLife.73456.
8. Ficiara E, Stura I, Guiot C. Iron deposition in brain: does aging matter? Int J Mol Sci. 2022;23(17):10018.
9. Qin Y, Zhu W, Zhan C, Zhao L, Wang J, Tian Q, et al. Investigation on positive correlation of increased brain iron deposition with cognitive impairment in Alzheimer disease by using quantitative MR R2' mapping. J Huazhong Univ Sci Technolog Med Sci. 2011;31(4):578.
10. van Duijn S, Bulk M, van Duinen SG, Nabuurs RJA, van Buchem MA, van der Weerd L, et al. Cortical iron reflects severity of Alzheimer's disease. J Alzheimers Dis. 2017;60(4):1533–45.
11. Spotorno N, Acosta-Cabronero J, Stomrud E, Lampinen B, Strandberg OT, van Westen D, et al. Relationship between cortical iron and tau aggregation in Alzheimer's disease. Brain. 2020;143(5):1341–9.
12. Connor JR, Menzies SL, St Martin SM, Mufson EJ. A histochemical study of iron, transferrin, and ferritin in Alzheimer's diseased brains. J Neurosci Res. 1992;31(1):75–83.
13. Meadowcroft MD, Connor JR, Smith MB, Yang QX. MRI and histological analysis of beta-amyloid plaques in both human Alzheimer's disease and APP/PS1 transgenic mice. J Magn Reson Imaging. 2009;29(5):997–1007.
14. Smith MA, Harris PL, Sayre LM, Perry G. Iron accumulation in Alzheimer disease is a source of redox-generated free radicals. Proc Natl Acad Sci U S A. 1997;94(18):9866–8.
15. Liu B, Moloney A, Meehan S, Morris K, Thomas SE, Serpell LC, et al. Iron promotes the toxicity of amyloid beta peptide by impeding its ordered aggregation. J Biol Chem. 2011;286(6):4248–56.
16. Rottkamp CA, Raina AK, Zhu X, Gaier E, Bush AI, Atwood CS, et al. Redox-active iron mediates amyloid-beta toxicity. Free Radic Biol Med. 2001;30(4):447–50.
17. Jomova K, Vondrakova D, Lawson M, Valko M. Metals, oxidative stress and neurodegenerative disorders. Mol Cell Biochem. 2010;345(1–2):91–104.
18. Hansen DV, Hanson JE, Sheng M. Microglia in Alzheimer's disease. J Cell Biol. 2018;217(2):459–72.
19. Hemonnot AL, Hua J, Ulmann L, Hirbec H. Microglia in Alzheimer disease: well-known targets and new opportunities. Front Aging Neurosci. 2019;11:233.
20. Nnah IC, Wessling-Resnick M. Brain iron homeostasis: a focus on microglial iron. Pharmaceuticals. 2018;11(4):129.
21. McIntosh A, Mela V, Harty C, Minogue AM, Costello DA, Kerskens C, et al. Iron accumulation in microglia triggers a cascade of events that leads to altered metabolism and compromised function in APP/PS1 mice. Brain Pathol. 2019;29(5):606–21.
22. Liu S, Gao X, Zhou S. New target for prevention and treatment of neuroinflammation: microglia iron accumulation and ferroptosis. ASN Neuro. 2022;14:17590914221133236.
23. Winn NC, Volk KM, Hasty AH. Regulation of tissue iron homeostasis: the macrophage "ferrostat." JCI Insight. 2020. https://doi.org/10.1172/jci.insight.132964.
24. McCarthy RC, Sosa JC, Gardeck AM, Baez AS, Lee CH, Wessling-Resnick M. Inflammation-induced iron transport and metabolism by brain microglia. J Biol Chem. 2018;293(20):7853–63.
25. Bishop GM, Dang TN, Dringen R, Robinson SR. Accumulation of non-transferrin-bound iron by neurons, astrocytes, and microglia. Neurotox Res. 2011;19(3):443–51.
26. Healy S, McMahon J, Owens P, FitzGerald U. Significant glial alterations in response to iron loading in a novel organotypic hippocampal slice culture model. Sci Rep. 2016;6:36410.
27. Reinert A, Morawski M, Seeger J, Arendt T, Reinert T. Iron concentrations in neurons and glial cells with estimates on ferritin concentrations. BMC Neurosci. 2019;20(1):25.
28. Jiao L, Li X, Luo Y, Wei J, Ding X, Xiong H, et al. Iron metabolism mediates microglia susceptibility in ferroptosis. Front Cell Neurosci. 2022;16:995084.
29. Ryan SK, Zelic M, Han Y, Teeple E, Chen L, Sadeghi M, et al. Microglia ferroptosis is regulated by SEC24B and contributes to neurodegeneration. Nat Neurosci. 2023;26(1):12–26.
30. Zeineh MM, Chen Y, Kitzler HH, Hammond R, Vogel H, Rutt BK. Activated iron-containing microglia in the human hippocampus identified by magnetic resonance imaging in Alzheimer disease. Neurobiol Aging. 2015;36(9):2483–500.
31. Kenkhuis B, Somarakis A, de Haan L, Dzyubachyk O, IJsselsteijn ME, de Miranda N, et al. Iron loading is a prominent feature of activated microglia in Alzheimer's disease patients. Acta Neuropathol Commun. 2021;9(1):27.
32. Holland R, McIntosh AL, Finucane OM, Mela V, Rubio-Araiz A, Timmons G, et al. Inflammatory microglia are glycolytic and iron retentive and typify the microglia in APP/PS1 mice. Brain Behav Immun. 2018;68:183–96.
33. Gillen KM, Mubarak M, Nguyen TD, Pitt D. Significance and in vivo detection of iron-laden microglia in white matter multiple sclerosis lesions. Front Immunol. 2018;9:255.
34. Adeniyi PA, Gong X, MacGregor E, Degener-O'Brien K, McClendon E, Garcia M, et al. Ferroptosis of microglia in aging human white matter injury. Ann Neurol. 2023. https://doi.org/10.1002/ana.26770.
35. Keren-Shaul H, Spinrad A, Weiner A, Matcovitch-Natan O, Dvir-Szternfeld R, Ulland TK, et al. A unique microglia type associated with restricting development of Alzheimer's disease. Cell. 2017;169(7):1276-90 e17.
36. Prater KE, Green KJ, Mamde S, Sun W, Cochoit A, Smith CL, et al. Human microglia show unique transcriptional changes in Alzheimer's disease. Nat Aging. 2023;3(7):894–907.
37. Ndayisaba A, Kaindlstorfer C, Wenning GK. Iron in neurodegeneration—cause or consequence? Front Neurosci. 2019;13:180.
38. Angelova DM, Brown DR. Microglia and the aging brain: are senescent microglia the key to neurodegeneration? J Neurochem. 2019;151(6):676–88.
39. Nnah IC, Lee CH, Wessling-Resnick M. Iron potentiates microglial interleukin-1beta secretion induced by amyloid-beta. J Neurochem. 2019. https://doi.org/10.1111/jnc.14906.
40. Yauger YJ, Bermudez S, Moritz KE, Glaser E, Stoica B, Byrnes KR. Iron accentuated reactive oxygen species release by NADPH oxidase in activated microglia contributes to oxidative stress in vitro. J Neuroinflammation. 2019;16(1):41.
41. Urrutia P, Aguirre P, Esparza A, Tapia V, Mena NP, Arredondo M, et al. Inflammation alters the expression of DMT1, FPN1 and hepcidin, and it causes iron accumulation in central nervous system cells. J Neurochem. 2013;126(4):541–9.
42. Volk Robertson K, Schleh MW, Harrison FE, Hasty AH. Microglial-specific knockdown of iron import gene, Slc11a2, blunts LPS-induced neuroinflammatory responses in a sex-specific manner. Brain Behav Immun. 2023;116:370–84.
43. Mims MP, Prchal JT. Divalent metal transporter 1. Hematology. 2005;10(4):339–45.
44. Shawki A, Knight PB, Maliken BD, Niespodzany EJ, Mackenzie B. H(+)-coupled divalent metal-ion transporter-1: functional properties, physiological roles and therapeutics. Curr Top Membr. 2012;70:169–214.
45. Nnah IC, Lee CH, Wessling-Resnick M. Iron potentiates microglial interleukin-1beta secretion induced by amyloid-beta. J Neurochem. 2020;154(2):177–89.
46. Yona S, Kim KW, Wolf Y, Mildner A, Varol D, Breker M, et al. Fate mapping reveals origins and dynamics of monocytes and tissue macrophages under homeostasis. Immunity. 2013;38(1):79–91.
47. Cheli VT, Santiago Gonzalez DA, Marziali LN, Zamora NN, Guitart ME, Spreuer V, et al. The divalent metal transporter 1 (DMT1) is required for iron uptake and normal development of oligodendrocyte progenitor cells. J Neurosci. 2018;38(43):9142–59.
48. Jankowsky JL, Fadale DJ, Anderson J, Xu GM, Gonzales V, Jenkins NA, et al. Mutant presenilins specifically elevate the levels of the 42 residue

beta-amyloid peptide in vivo: evidence for augmentation of a 42-specific gamma secretase. Hum Mol Genet. 2004;13(2):159–70.
49. Izco M, Martinez P, Corrales A, Fandos N, Garcia S, Insua D, et al. Changes in the brain and plasma Abeta peptide levels with age and its relationship with cognitive impairment in the APPswe/PS1dE9 mouse model of Alzheimer's disease. Neuroscience. 2014;263:269–79.
50. Yan P, Bero AW, Cirrito JR, Xiao Q, Hu X, Wang Y, et al. Characterizing the appearance and growth of amyloid plaques in APP/PS1 mice. J Neurosci. 2009;29(34):10706–14.
51. Peters DG, Connor JR, Meadowcroft MD. The relationship between iron dyshomeostasis and amyloidogenesis in Alzheimer's disease: two sides of the same coin. Neurobiol Dis. 2015;81:49–65.
52. Willis EF, Vukovic J. Protocol for brain-wide or region-specific microglia depletion and repopulation in adult mice. STAR Protoc. 2020;1(3):100211.
53. Sahasrabuddhe V, Ghosh HS. Cx3Cr1-Cre induction leads to microglial activation and IFN-1 signaling caused by DNA damage in early postnatal brain. Cell Rep. 2022;38(3):110252.
54. Faust TE, Feinberg PA, O'Connor C, Kawaguchi R, Chan A, Strasburger H, et al. A comparative analysis of microglial inducible Cre lines. Cell Rep. 2023;42(9):113031.
55. Reyes-Marin KE, Nunez A. Seizure susceptibility in the APP/PS1 mouse model of Alzheimer's disease and relationship with amyloid beta plaques. Brain Res. 2017;1677:93–100.
56. Deacon RM. Assessing nest building in mice. Nat Protoc. 2006;1(3):1117–9.
57. Consoli DC, Spitznagel BD, Owen BM, Kang H, Williams Roberson S, Pandharipande P, et al. Altered EEG, disrupted hippocampal long-term potentiation and neurobehavioral deficits implicate a delirium-like state in a mouse model of sepsis. Brain Behav Immun. 2023;107:165–78.
58. Nunez J. Morris water maze experiment. J Vis Exp. 2008. https://doi.org/10.3791/897-v.
59. Grabert K, McColl BW. Isolation and phenotyping of adult mouse microglial cells. Methods Mol Biol. 2018;1784:77–86.
60. Lee JK, Tansey MG. Microglia isolation from adult mouse brain. Methods Mol Biol. 2013;1041:17–23.
61. Bordt EA, Block CL, Petrozziello T, Sadri-Vakili G, Smith CJ, Edlow AG, et al. Isolation of microglia from mouse or human tissue. STAR Protoc. 2020;1(1):100035.
62. McCarthy RC, Lu DY, Alkhateeb A, Gardeck AM, Lee CH, Wessling-Resnick M. Characterization of a novel adult murine immortalized microglial cell line and its activation by amyloid-beta. J Neuroinflammation. 2016;13:21.
63. Wetli HA, Buckett PD, Wessling-Resnick M. Small-molecule screening identifies the selanazal drug ebselen as a potent inhibitor of DMT1-mediated iron uptake. Chem Biol. 2006;13(9):965–72.
64. Rhee JW, Yi H, Thomas D, Lam CK, Belbachir N, Tian L, et al. Modeling secondary iron overload cardiomyopathy with human induced pluripotent stem cell-derived cardiomyocytes. Cell Rep. 2020;32(2):107886.
65. Kenkhuis B, van Eekeren M, Parfitt DA, Ariyurek Y, Banerjee P, Priller J, et al. Iron accumulation induces oxidative stress, while depressing inflammatory polarization in human iPSC-derived microglia. Stem Cell Rep. 2022;17(6):1351–65.
66. Livak KJ, Schmittgen TD. Analysis of relative gene expression data using real-time quantitative PCR and the 2(-Delta Delta C(T)) method. Methods. 2001;25(4):402–8.
67. Felix Krueger F, James, Phil Ewels, Ebrahim Afyounian, Michael Weinstein, Benjamin Schuster-Boeckler, Gert Hulselmans, & scalmons. FelixKrueger/TrimGalore: v0.6.10—add default decompression path (0.6.10) Zenodo. 2023.
68. Martin M. Cutadapt removes adapter sequences from high-throughput sequencing reads. EMBnetjournal. 2011;17(1):10–2.
69. Dobin A, Davis CA, Schlesinger F, Drenkow J, Zaleski C, Jha S, et al. STAR: ultrafast universal RNA-seq aligner. Bioinformatics. 2013;29(1):15–21.
70. Love MI, Huber W, Anders S. Moderated estimation of fold change and dispersion for RNA-seq data with DESeq2. Genome Biol. 2014;15(12):550.
71. Subramanian A, Tamayo P, Mootha VK, Mukherjee S, Ebert BL, Gillette MA, et al. Gene set enrichment analysis: a knowledge-based approach for interpreting genome-wide expression profiles. Proc Natl Acad Sci U S A. 2005;102(43):15545–50.
72. Yu G, Wang LG, Han Y, He QY. clusterProfiler: an R package for comparing biological themes among gene clusters. OMICS. 2012;16(5):284–7.
73. Castanza AS, Recla JM, Eby D, Thorvaldsdottir H, Bult CJ, Mesirov JP. Extending support for mouse data in the molecular signatures database (MSigDB). Nat Methods. 2023;20(11):1619–20.
74. Song Y, Wang J. ggcoverage: an R package to visualize and annotate genome coverage for various NGS data. BMC Bioinform. 2023;24(1):309.
75. Lopes KO, Sparks DL, Streit WJ. Microglial dystrophy in the aged and Alzheimer's disease brain is associated with ferritin immunoreactivity. Glia. 2008;56(10):1048–60.
76. Gunshin H, Fujiwara Y, Custodio AO, Direnzo C, Robine S, Andrews NC. Slc11a2 is required for intestinal iron absorption and erythropoiesis but dispensable in placenta and liver. J Clin Invest. 2005;115(5):1258–66.
77. Carlson ES, Tkac I, Magid R, O'Connor MB, Andrews NC, Schallert T, et al. Iron is essential for neuron development and memory function in mouse hippocampus. J Nutr. 2009;139(4):672–9.
78. Hopperton KE, Mohammad D, Trepanier MO, Giuliano V, Bazinet RP. Markers of microglia in post-mortem brain samples from patients with Alzheimer's disease: a systematic review. Mol Psychiatry. 2018;23(2):177–98.
79. March-Diaz R, Lara-Urena N, Romero-Molina C, Heras-Garvin A, Ortega-de San Luis C, Alvarez-Vergara MI, et al. Hypoxia compromises the mitochondrial metabolism of Alzheimer's disease microglia via HIF1. Nat Aging. 2021;1(4):385–99.
80. Holtman IR, Raj DD, Miller JA, Schaafsma W, Yin Z, Brouwer N, et al. Induction of a common microglia gene expression signature by aging and neurodegenerative conditions: a co-expression meta-analysis. Acta Neuropathol Commun. 2015;3:31.
81. Marschallinger J, Iram T, Zardeneta M, Lee SE, Lehallier B, Haney MS, et al. Lipid-droplet-accumulating microglia represent a dysfunctional and proinflammatory state in the aging brain. Nat Neurosci. 2020;23(2):194–208.
82. Wang Y, Luo W, Wang X, Ma Y, Huang L, Wang Y. MAMDC2, a gene highly expressed in microglia in experimental models of Alzheimers disease, positively regulates the innate antiviral response during neurotropic virus infection. J Infect. 2022;84(2):187–204.
83. Chen Y, Colonna M. Microglia in Alzheimer's disease at single-cell level. Are there common patterns in humans and mice? J Exp Med. 2021;218(9): e20202717.
84. Xu YJ, Au NPB, Ma CHE. Functional and phenotypic diversity of microglia: implication for microglia-based therapies for Alzheimer's disease. Front Aging Neurosci. 2022;14:896852.
85. Rangaraju S, Dammer EB, Raza SA, Rathakrishnan P, Xiao H, Gao T, et al. Identification and therapeutic modulation of a pro-inflammatory subset of disease-associated-microglia in Alzheimer's disease. Mol Neurodegener. 2018;13(1):24.
86. Deczkowska A, Keren-Shaul H, Weiner A, Colonna M, Schwartz M, Amit I. Disease-associated microglia: a universal immune sensor of neurodegeneration. Cell. 2018;173(5):1073–81.
87. Wei Y, Li X. Different phenotypes of microglia in animal models of Alzheimer disease. Immun Ageing. 2022;19(1):44.
88. Wang H. Microglia heterogeneity in Alzheimer's disease: insights from single-cell technologies. Front Synaptic Neurosci. 2021;13:773590.
89. Kwiatek-Majkusiak J, Dickson DW, Tacik P, Aoki N, Tomasiuk R, Koziorowski D, et al. Relationships between typical histopathological hallmarks and the ferritin in the hippocampus from patients with Alzheimer's disease. Acta Neurobiol Exp. 2015;75(4):391–8.
90. Levi S, Ripamonti M, Moro AS, Cozzi A. Iron imbalance in neurodegeneration. Mol Psychiatry. 2024. https://doi.org/10.1038/s41380-023-02399-z.
91. Simmons DA, Casale M, Alcon B, Pham N, Narayan N, Lynch G. Ferritin accumulation in dystrophic microglia is an early event in the development of Huntington's disease. Glia. 2007;55(10):1074–84.
92. Mathys H, Davila-Velderrain J, Peng Z, Gao F, Mohammadi S, Young JZ, et al. Single-cell transcriptomic analysis of Alzheimer's disease. Nature. 2019;570(7761):332–7.

93. Angelova DM, Brown DR. Model senescent microglia induce disease related changes in alpha-synuclein expression and activity. Biomolecules. 2018;8(3):67.
94. Niraula A, Sheridan JF, Godbout JP. Microglia priming with aging and stress. Neuropsychopharmacology. 2017;42(1):318–33.
95. Norden DM, Godbout JP. Review: microglia of the aged brain: primed to be activated and resistant to regulation. Neuropathol Appl Neurobiol. 2013;39(1):19–34.
96. Salazar J, Mena N, Hunot S, Prigent A, Alvarez-Fischer D, Arredondo M, et al. Divalent metal transporter 1 (DMT1) contributes to neurodegeneration in animal models of Parkinson's disease. Proc Natl Acad Sci U S A. 2008;105(47):18578–83.
97. Lee HP, Zhu X, Liu G, Chen SG, Perry G, Smith MA, et al. Divalent metal transporter, iron, and Parkinson's disease: a pathological relationship. Cell Res. 2010;20(4):397–9.
98. Tag SH, Kim B, Bae J, Chang KA, Im HI. Neuropathological and behavioral features of an APP/PS1/MAPT (6xTg) transgenic model of Alzheimer's disease. Mol Brain. 2022;15(1):51.
99. Ferguson SA, Sarkar S, Schmued LC. Longitudinal behavioral changes in the APP/PS1 transgenic Alzheimer's disease model. Behav Brain Res. 2013;242:125–34.
100. Shepherd A, May C, Churilov L, Adlard PA, Hannan AJ, Burrows EL. Evaluation of attention in APP/PS1 mice shows impulsive and compulsive behaviours. Genes Brain Behav. 2021;20(1): e12594.
101. Wang T, Chen Y, Zou Y, Pang Y, He X, Chen Y, et al. Locomotor hyperactivity in the early-stage Alzheimer's disease-like pathology of APP/PS1 mice: associated with impaired polarization of astrocyte aquaporin 4. Aging Dis. 2022;13(5):1504–22.
102. Jul P, Volbracht C, de Jong IE, Helboe L, Elvang AB, Pedersen JT. Hyperactivity with agitative-like behavior in a mouse tauopathy model. J Alzheimers Dis. 2016;49(3):783–95.
103. Oblak AL, Lin PB, Kotredes KP, Pandey RS, Garceau D, Williams HM, et al. Comprehensive evaluation of the 5XFAD mouse model for preclinical testing applications: a MODEL-AD study. Front Aging Neurosci. 2021;13:713726.
104. Fernandez M, Gobartt AL, Balana M, Group CS. Behavioural symptoms in patients with Alzheimer's disease and their association with cognitive impairment. BMC Neurol. 2010;10:87.
105. Zhou H, Li H, Gowravaram N, Quan M, Kausar N, Gomperts SN. Disruption of hippocampal neuronal circuit function depends upon behavioral state in the APP/PS1 mouse model of Alzheimer's disease. Sci Rep. 2022;12(1):21022.
106. Melnikova T, Savonenko A, Wang Q, Liang X, Hand T, Wu L, et al. Cycloxygenase-2 activity promotes cognitive deficits but not increased amyloid burden in a model of Alzheimer's disease in a sex-dimorphic pattern. Neuroscience. 2006;141(3):1149–62.
107. Miki Stein A, Munive V, Fernandez AM, Nunez A, Torres AI. Acute exercise does not modify brain activity and memory performance in APP/PS1 mice. PLoS ONE. 2017;12(5): e0178247.
108. Brandeis R, Brandys Y, Yehuda S. The use of the Morris Water Maze in the study of memory and learning. Int J Neurosci. 1989;48(1–2):29–69.
109. Maren S, Phan KL, Liberzon I. The contextual brain: implications for fear conditioning, extinction and psychopathology. Nat Rev Neurosci. 2013;14(6):417–28.
110. Knafo S, Venero C, Merino-Serrais P, Fernaud-Espinosa I, Gonzalez-Soriano J, Ferrer I, et al. Morphological alterations to neurons of the amygdala and impaired fear conditioning in a transgenic mouse model of Alzheimer's disease. J Pathol. 2009;219(1):41–51.
111. Tovote P, Fadok JP, Luthi A. Neuronal circuits for fear and anxiety. Nat Rev Neurosci. 2015;16(6):317–31.
112. Poulin SP, Dautoff R, Morris JC, Barrett LF, Dickerson BC, Alzheimer's Disease Neuroimaging I. Amygdala atrophy is prominent in early Alzheimer's disease and relates to symptom severity. Psychiatry Res. 2011;194(1):7–13.
113. Prieto Del Val L, Cantero JL, Atienza M. Atrophy of amygdala and abnormal memory-related alpha oscillations over posterior cingulate predict conversion to Alzheimer's disease. Sci Rep. 2016;6:31859.
114. Lin TW, Liu YF, Shih YH, Chen SJ, Huang TY, Chang CY, et al. Neurodegeneration in amygdala precedes hippocampus in the APPswe/PS1dE9 mouse model of Alzheimer's disease. Curr Alzheimer Res. 2015;12(10):951–63.
115. Kitamura J, Nagai M, Ueno H, Ohshita T, Kikumoto M, Toko M, et al. The insular cortex, Alzheimer disease pathology, and their effects on blood pressure variability. Alzheimer Dis Assoc Disord. 2020;34(3):282–91.
116. Bonthius DJ, Solodkin A, Van Hoesen GW. Pathology of the insular cortex in Alzheimer disease depends on cortical architecture. J Neuropathol Exp Neurol. 2005;64(10):910–22.
117. Rosenberg PB, Nowrangi MA, Lyketsos CG. Neuropsychiatric symptoms in Alzheimer's disease: what might be associated brain circuits? Mol Aspects Med. 2015;43–44:25–37.
118. Beam CR, Kaneshiro C, Jang JY, Reynolds CA, Pedersen NL, Gatz M. Differences between women and men in incidence rates of dementia and Alzheimer's disease. J Alzheimers Dis. 2018;64(4):1077–83.
119. Podcasy JL, Epperson CN. Considering sex and gender in Alzheimer disease and other dementias. Dialogues Clin Neurosci. 2016;18(4):437–46.
120. Li X, Feng Y, Wu W, Zhao J, Fu C, Li Y, et al. Sex differences between APPswePS1dE9 mice in A-beta accumulation and pancreatic islet function during the development of Alzheimer's disease. Lab Anim. 2016;50(4):275–85.
121. Wang J, Tanila H, Puolivali J, Kadish I, van Groen T. Gender differences in the amount and deposition of amyloidbeta in APPswe and PS1 double transgenic mice. Neurobiol Dis. 2003;14(3):318–27.
122. Yang JT, Wang ZJ, Cai HY, Yuan L, Hu MM, Wu MN, et al. Sex differences in neuropathology and cognitive behavior in APP/PS1/tau triple-transgenic mouse model of Alzheimer's disease. Neurosci Bull. 2018;34(5):736–46.
123. Jiao SS, Bu XL, Liu YH, Zhu C, Wang QH, Shen LL, et al. Sex dimorphism profile of Alzheimer's disease-type pathologies in an APP/PS1 mouse model. Neurotox Res. 2016;29(2):256–66.
124. Bartzokis G, Tishler TA, Lu PH, Villablanca P, Altshuler LL, Carter M, et al. Brain ferritin iron may influence age- and gender-related risks of neurodegeneration. Neurobiol Aging. 2007;28(3):414–23.
125. Bartzokis G, Tishler TA, Shin IS, Lu PH, Cummings JL. Brain ferritin iron as a risk factor for age at onset in neurodegenerative diseases. Ann N Y Acad Sci. 2004;1012:224–36.
126. Chung SD, Sheu JJ, Kao LT, Lin HC, Kang JH. Dementia is associated with iron-deficiency anemia in females: a population-based study. J Neurol Sci. 2014;346(1–2):90–3.
127. Whitfield JB, Treloar S, Zhu G, Powell LW, Martin NG. Relative importance of female-specific and non-female-specific effects on variation in iron stores between women. Br J Haematol. 2003;120(5):860–6.
128. Andreeva VA, Galan P, Arnaud J, Julia C, Hercberg S, Kesse-Guyot E. Midlife iron status is inversely associated with subsequent cognitive performance, particularly in perimenopausal women. J Nutr. 2013;143(12):1974–81.
129. Hahn P, Song Y, Ying GS, He X, Beard J, Dunaief JL. Age-dependent and gender-specific changes in mouse tissue iron by strain. Exp Gerontol. 2009;44(9):594–600.
130. Palsa K, Neely EB, Baringer SL, Helmuth TB, Simpson IA, Connor JR. Brain iron acquisition depends on age and sex in iron-deficient mice. FASEB J. 2024;38(1): e23331.
131. Lynch MA. Exploring sex-related differences in microglia may be a game-changer in precision medicine. Front Aging Neurosci. 2022;14:868448.
132. Guillot-Sestier MV, Araiz AR, Mela V, Gaban AS, O'Neill E, Joshi L, et al. Microglial metabolism is a pivotal factor in sexual dimorphism in Alzheimer's disease. Commun Biol. 2021;4(1):711.
133. Han J, Fan Y, Zhou K, Blomgren K, Harris RA. Uncovering sex differences of rodent microglia. J Neuroinflammation. 2021;18(1):74.
134. Sullivan O, Ciernia AV. Work hard, play hard: how sexually differentiated microglia work to shape social play and reproductive behavior. Front Behav Neurosci. 2022;16:989011.
135. Huang E, Ong WY, Go ML, Connor JR. Upregulation of iron regulatory proteins and divalent metal transporter-1 isoforms in the rat hippocampus after kainate induced neuronal injury. Exp Brain Res. 2006;170(3):376–86.
136. Ingrassia R, Lanzillotta A, Sarnico I, Benarese M, Blasi F, Borgese L, et al. 1B/(-)IRE DMT1 expression during brain ischemia contributes to cell

death mediated by NF-kappaB/RelA acetylation at Lys310. PLoS ONE. 2012;7(5): e38019.
137. Friedman BA, Srinivasan K, Ayalon G, Meilandt WJ, Lin H, Huntley MA, et al. Diverse brain myeloid expression profiles reveal distinct microglial activation states and aspects of Alzheimer's disease not evident in mouse models. Cell Rep. 2018;22(3):832–47.
138. Stankiewicz AM, Goscik J, Majewska A, Swiergiel AH, Juszczak GR. The effect of acute and chronic social stress on the hippocampal transcriptome in mice. PLoS ONE. 2015;10(11): e0142195.
139. Sousa JC, Cardoso I, Marques F, Saraiva MJ, Palha JA. Transthyretin and Alzheimer's disease: where in the brain? Neurobiol Aging. 2007;28(5):713–8.
140. Shippy DC, Watters JJ, Ulland TK. Transcriptional response of murine microglia in Alzheimer's disease and inflammation. BMC Genom. 2022;23(1):183.
141. Li X, Buxbaum JN. Transthyretin and the brain re-visited: is neuronal synthesis of transthyretin protective in Alzheimer's disease? Mol Neurodegener. 2011;6:79.
142. Sobue A, Komine O, Hara Y, Endo F, Mizoguchi H, Watanabe S, et al. Microglial gene signature reveals loss of homeostatic microglia associated with neurodegeneration of Alzheimer's disease. Acta Neuropathol Commun. 2021;9(1):1.
143. Jiang L, Mu H, Xu F, Xie D, Su W, Xu J, et al. Transcriptomic and functional studies reveal undermined chemotactic and angiostimulatory properties of aged microglia during stroke recovery. J Cereb Blood Flow Metab. 2020;40(1_suppl):S81–97.
144. Amaral RF, Geraldo LHM, Einicker-Lamas M, eSpohr TCLS, Mendes F, Lima FRS. Microglial lysophosphatidic acid promotes glioblastoma proliferation and migration via LPA(1) receptor. J Neurochem. 2021;156(4):499–512.
145. Lastres-Becker I, Innamorato NG, Jaworski T, Rabano A, Kugler S, Van Leuven F, et al. Fractalkine activates NRF2/NFE2L2 and heme oxygenase 1 to restrain tauopathy-induced microgliosis. Brain. 2014;137(Pt 1):78–91.
146. Boche D, Gordon MN. Diversity of transcriptomic microglial phenotypes in aging and Alzheimer's disease. Alzheimers Dement. 2022;18(2):360–76.
147. Nguyen AT, Wang K, Hu G, Wang X, Miao Z, Azevedo JA, et al. APOE and TREM2 regulate amyloid-responsive microglia in Alzheimer's disease. Acta Neuropathol. 2020;140(4):477–93.
148. Krasemann S, Madore C, Cialic R, Baufeld C, Calcagno N, El Fatimy R, et al. The TREM2-APOE pathway drives the transcriptional phenotype of dysfunctional microglia in neurodegenerative diseases. Immunity. 2017;47(3):566-81 e9.
149. Sebastian Monasor L, Muller SA, Colombo AV, Tanrioever G, Konig J, Roth S, et al. Fibrillar Abeta triggers microglial proteome alterations and dysfunction in Alzheimer mouse models. Elife. 2020;9: e54083.
150. Ghazaiean M, Aliasgharian A, Karami H, Darvishi-Khezri H. Ebselen: a promising therapy protecting cardiomyocytes from excess iron in iron-overloaded thalassemia patients. Open Med. 2023;18(1):20230733.
151. Landgraf AD, Alsegiani AS, Alaqel S, Thanna S, Shah ZA, Sucheck SJ. Neuroprotective and Anti-neuroinflammatory properties of ebselen derivatives and their potential to inhibit neurodegeneration. ACS Chem Neurosci. 2020;11(19):3008–16.
152. Ren X, Zou L, Lu J, Holmgren A. Selenocysteine in mammalian thioredoxin reductase and application of ebselen as a therapeutic. Free Radic Biol Med. 2018;127:238–47.
153. Martini F, Rosa SG, Klann IP, Fulco BCW, Carvalho FB, Rahmeier FL, et al. A multifunctional compound ebselen reverses memory impairment, apoptosis and oxidative stress in a mouse model of sporadic Alzheimer's disease. J Psychiatr Res. 2019;109:107–17.
154. Xie L, Zheng W, Xin N, Xie JW, Wang T, Wang ZY. Ebselen inhibits iron-induced tau phosphorylation by attenuating DMT1 up-regulation and cellular iron uptake. Neurochem Int. 2012;61(3):334–40.
155. Davis MT, Bartfay WJ. Ebselen decreases oxygen free radical production and iron concentrations in the hearts of chronically iron-overloaded mice. Biol Res Nurs. 2004;6(1):37–45.
156. Mukem S, Sayoh I, Maungchanburi S, Thongbuakaew T. Ebselen, iron uptake inhibitor, alleviates iron overload-induced senescence-like neuronal cells SH-SY5Y via suppressing the mTORC1 signaling pathway. Adv Pharmacol Pharm Sci. 2023;2023:6641347.
157. Lingappan K. NF-kappaB in oxidative stress. Curr Opin Toxicol. 2018;7:81–6.
158. Ward RJ, Zucca FA, Duyn JH, Crichton RR, Zecca L. The role of iron in brain ageing and neurodegenerative disorders. Lancet Neurol. 2014;13(10):1045–60.
159. Lee CY, Landreth GE. The role of microglia in amyloid clearance from the AD brain. J Neural Transm. 2010;117(8):949–60.
160. Swanson MEV, Mrkela M, Murray HC, Cao MC, Turner C, Curtis MA, et al. Microglial CD68 and L-ferritin upregulation in response to phosphorylated-TDP-43 pathology in the amyotrophic lateral sclerosis brain. Acta Neuropathol Commun. 2023;11(1):69.

Publisher's Note

Katrina Volk Robertson is now a Visiting Assistant Professor at Pepperdine University in Malibu, CA.

Alyssa H. Hasty is now Vice-Provost and Senior Associate Dean for Faculty Affairs and Career Development at University of Texas Southwestern in Dallas, TX.